University of Peloponnese

Department of History, Archaeology and Cultural Resources Management

Master of Science
in Cultural Heritage Materials and Technologies

The Catania Project

2D, 3D XRF microanalysis of Roman wall-paintings

MSc Thesis

by Savvina Fotiou

Supervisors:

Dr. A. G. Karydas of N.C.S.R. "Demokritos"

Prof. N. Zacharias of University of Peloponnese

Dr. P. F. Romano of I.N.F.N

Kalamata 2019

Contents

1 Abstract

In this thesis three different modalities of XRF analytical techniques are performed on roman wall – painting fragments for pigment identification and exploration of paint-layer stratigraphy. Seven wall – painting fragments originated from two roman houses located in Sicily of Italy are analyzed. The techniques that were used for their analysis include 1D (depth), 2D (area) and 3D (volume) scan measurements performed by a micro confocal XRF system.

The XRF results from the analysis of the roman wall – painting fragments have identified the application of the following pigments on a lime-based substrate: ochre, green earth, cinnabar, Cu based green (malachite /verdigris) and blue pigments (azurite). For certain pigments, specific elemental associations have been revealed between major and minor elements. Through the application of the 1D (depth) and 3D (volume) XRF methodologies the thickness of each paint layer as well as the paint stratigraphy of each sample is investigated. The in-depth (1D) elemental profiles of calcium coming from the preparation layer usually appears in the same depth with the paint layers pigments. It is not clear if that is the way that calcium behaves at different conditions and passing of the time or if Romans used a lime solution or just water to apply their pigments. Further systematic work is needed to better understand the ancient recipes and to evaluate possible degradation pathways.

2   Acknowledgements

3   Introduction

Nowadays more and more archaeometric studies are carried out on Roman wall – paintings to determine the constituent materials and the techniques of their application using complementary analytical techniques.

The chemical analysis of archaeological and historical museum objects is essential for better understanding of ancient materials and techniques. To know the chemical composition of the painted layers of an ancient mural can be useful to understand the methods of manufacturing (Bardelli *et al.*, 2011), or the geographical spread of materials or cultural objects. Also, through scientific methods it is able to evaluate the state of conservation which will lead to the adoption of the most suitable conservation treatment (Caliri, 2017). It needs to be clear that archaeological objects are irreplaceable, so the use of non-destructive analytical techniques are considered necessary for their investigation and analysis.

X-ray Fluorescence (XRF) is a non-destructive, fast, versatile and multi-elemental method of analysis that does not require sampling (Haschke, 2014). Some applications of XRF, like handheld or portable XRF do not even require moving of the object. Through the method of XRF it is possible to gain information about the preservation state of an object (Woldseth, 1973), as well as tackling issues related with authenticity, provenance, historical, chronological, geographical and social background (Mahnke, 2014).

For this thesis, wall – painting fragments from two Roman sites in Sicily are analyzed to determine the pigments and the application techniques used for their manufacturing through the utilization of three different modalities of the micro-XRF analytical technique.

3.1   Principles of XRF analysis

X-ray fluorescence is the most widely used analytical technique used in works of art and other cultural heritage materials (Trentelman *et al*. 2010). The technique is based on Moseley's law (*Figure 1*).

[1]

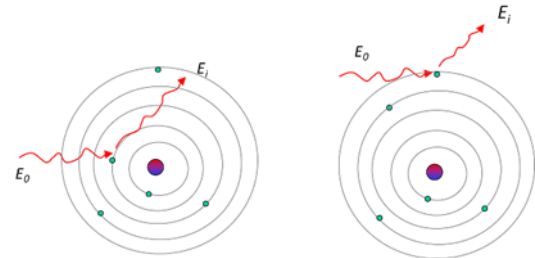$$\sqrt{\frac{v}{R}} = \frac{Z - S_n}{n}$$

Figure 1 Moseley's law (Musílek, Čechák and Trojek, 2012)

Figure 2 X-ray Scattering Interactions with atoms

XRF is a spectroscopic analysis method based on the emission of the "characteristic" or fluorescence x-ray radiation emitted from the elements contained in the material or sample when it is irradiated by X-rays. An X-ray tube produces X-rays which irradiate the object/sample and causes photo-ionization of inner atomic shells. This mechanism causes the ejection of an electron from the respective inner-shell of the atom, which proceeds to relaxation to the minimum energy by filling the created hole with an electron from one of its upper sub-shells (*Figure 2*). The relaxation/decay process of the ionized atom through the allowed electronic transitions is accompanied with certain probability (expressed by the so-called fluorescence yield) with the emission of characteristic X-ray radiation-fluorescence which can be detected by an energy dispersive X-ray detector attached to the XRF system. The energy of the characteristic X-ray is specific for each element depending on its atomic number (Z) (Mahnke, 2014). The energy of the exciting X-ray beam must be adequate to ionize the atomic inner-shell electrons of the elements of interest. The concentrations of the measured elements can be determined from the peak intensities of the corresponding spectral lines (Musílek, Čechák and Trojek, 2012). XRF analysis is sensitive to analyze and quantify most of the periodic table elements (mainly from sodium with Z=11 up to Z=92) (Janssens *et al.*, 2013).

---

[1]   V= the frequency of the characteristic X-rays
R= Rydeberg constant
n= quantum number of the corresponding electron shell
Z= atomic number
Sn= the screening factor (Musílek, Čechák and Trojek, 2012)

For the complete understanding of the XRF methodology it is crucial for a researcher to understand all the phenomena that take place during an object's XRF analysis. When an exciting X-ray beam irradiates an object five different phenomena may occur:. the incident beam and characteristic radiation absorption within the sample, Rayleigh (elastic) scattering, Compton (inelastic) scattering, diffraction and X-ray fluorescence (Shugar and Mass 2012). Since most of these phenomena are visible within the energy dispersive spectra, the analyst should be able to identify them to achieve an appropriate interpretation and spectrum analysis results.

3.2 XRF instrumentation

An XRF instrument is composed by an X-ray tube that produces the exciting X-rays, an optic or a pair of optics (depending the variant of the XRF instrument) that focuses the exciting beam (micro-XRF instrument) and in addition could accept from a specific analysis micro volume the fluorescence radiation (confocal micro-XRF set-up) and an energy dispersive detector that measures the characteristic radiation that emanates from the irradiated sample.

In X-ray tubes there are an anode and a metallic cathode. Within the tube a constant flux of accelerated electrons is emitted by the cathode moving towards the tube anode under vacuum conditions (Caliri, 2017). X-ray tubes are made of materials like glass, metal or ceramic and the materials used for the manufacturing of the anode are usually Rhodium (Rh), Molybdenum (Mo), Tungsten (W), Copper (Cu) or Chromium (Cr) (Haschke, 2014). The X-ray tube spectrum is comprised by two spectral components. A continuum energy distribution up to the maximum kinetic energy of the accelerated electrons produced due to the inelastic collisions of the energetic electrons with the electronic atomic environment of the anode and which progressively slow down the electrons beam. This component is called bremsstrahlung radiation. The energetic electron beam can also produce inner shell ionization of the anode atoms, thus inducing the emission of the anode characteristic radiation. However, most of the accelerated electron beam energy is converted into heat increasing the local temperature of the anode material.

Primary X-ray optics are usually placed between the X-ray source and the sample. They are used to shape the beam of the X-ray source and influence its energy distribution. They are of different typology: monocapillaries, cylindrical, ellipsoidal or paraboloidal capillaries or polycapillaries (Caliri, 2017). Polycapillary optics can be used in several types of X-ray analyses in order to increase the performance of the technique. The beam size of the optics can reach down to 10 μm (Wolff *et al.*, 2009). Polycapillary optics can focus the divergent exciting radiation from an X-ray source into the micrometer regime or oppositely, can capture the radiation emitted from a restrited source dimensions and produce a parallel beam. They allow to perform local analysis in high spatial resolution (Caliri, 2017). Such a lens is made by bundles of thousands of individual capillaries, which are bent hollow capillary channels. They are organized in the shape of hexagon honeycombs and settled all together again as a honeycomb (Haschke, 2014). They are distinguished in full and half lenses. Full lenses concentrate the radiation in a small spot while half lenses allow for the radiation to exit when all the individual X-rays that propagate from every single capillary are parallel. Polycapillary lenses are made mainly of glass. The propagation of X-rays through the lenses is governed by the phenomenon of total external reflection. The characteristic X-rays of low and medium atomic number elements are guided through the external and middle bundles of the optic, while characteristic X-rays of higher atomic number elements are guided mostly through the middle bundles.

A secondary optics (half lens instead of a full lens) can be placed between the sample and the detector. (Haschke, 2014)

The characteristic X-rays emitted from the elements analyzed are detected through the conversion of their energy to an electrical signal - within a semiconductor crystal (usually silicon) (Caliri, 2017). . The common energy dispersive detectors used in X-ray spectroscopy are Si(Li) detectors, PIN-diode detectors and silicon drift detectors (SDD). SDDs are made by high purity silicon with very low leakage current and are widely preferred nowadays due to their, very low capacitance that offers excellent energy resolution even at very high input count rates (Caliri, 2017),

3.3   Macroscopic XRF imaging

In order to investigate larger areas of a single object/artwork mostly for the purpose of visualizing any painted sub-surfaces of the object/artwork, XRF imaging techniques

were developed. XRF imaging can provide the user, either that is a conservator or an archaeologist with results in the form of 2 dimensional (2D) images that are better comprehensible. The X-rays irradiate the object in the same way as in the typical XRF technique causing the emission of fluorescence radiation from the constituent elements. The object/artwork or the spectrometer head moves gradually from one spot to its neighboring with a discrete step or continuous movement and as a result a whole area is scanned (Caliri, 2017). From each measurement an individual spot spectrum is produced. This procedure allows the display of the intensity changes along the scanned area, where color coding is applied for several elements. The color intensity is marked by the color brightness especially when it comes for the overlays of different elements distributions (Haschke, 2014). This variant of XRF is called macroscopic XRF analysis (MA-XRF). MA-XRF can determine the distribution of pigments on colored works of art or antiquities over large areas (Janssens *et al.*, 2013) using a beam with size of about few hundred of microns up to 1 mm (Caliri, 2017).

However, when XRF analysis in micrometric scale is required another variant of XRF can be used, the so-called micro XRF analysis (μXRF). μXRF can obtain information about the local elemental composition of inhomogeneous samples within a very small area using a micrometric beam size in the range of tens of microns (Caliri, 2017), (Janssens *et al.*, 2013).

The two previous techniques can be combined to allow MA-XRF imaging with micrometric spatial resolution. This can be achieved by readjusting the distance of the exit of the X-ray lens with respect to the object's/artwork's surface to provide an optimum spatial resolution for the tube exciting beam. This methodology is mostly used for the investigation of smaller details within a painted surface offering a better knowledge of the composition and painting technique. (Caliri, 2017)

3.4   Confocal XRF analysis & 3D micro-XRF imaging

Another useful variant of XRF analysis is the confocal micro-XRF analysis (Kanngießer *et al.*, 2012). It is based on the creation of a complex geometrical arrangement (confocal geometry) constituted by two focusing optics (Haschke, 2014). The two optics are arranged both in the excitation and the detection channel and their overlap creating a micro volume. Through this micro volume which is constant with respect to the instrument, the chemical composition of an object can be examined not

only across its surface (defined by the xy plane), but also through the perpendicular to the object axis (depth), as it moves back and forth towards the instrument with a few micrometer step (Kanngießer, Malzer and Reiche, 2003). In general, this set-up arrangement of X-ray optics can generate results in 1 to 3 dimensions. The intensity of the elements' signal is less than the ones in 2D measurements due to the small volume of the radiation that is collected (Haschke, 2014). In addition, the detected fluorescence intensity varies for every different layer of the sample due to the absorption of the exciting radiation to each layer but also due the absorption of the characteristic radiation that emanates from each layer towards the detector (Haschke, 2014). The absorption effect depends on the composition and density of each layer of the sample.

.

Through the use of a confocal micro-XRF arrangement measurements in all three coordinates of the sample dimensions (x, y and z) can be performed thus creating a 3D elemental image of the object within a micrometric regime (Nakano and Tsuji, 2010). Through the use of specialized programs, all the pixel spectra obtained can be analyzed through a batching process, whereas the rendering of all results can be visualized in 3D models with color coding that reveal the 3D distribution and concentration of each element measured.

3.5   XRF analysis of wall-painting pigments

The investigation of pigments provides significant information for defining the gamut of pigments available at a local, regional or even wider scale, and so for discovering the lines of communication and trade exchange. With XRF it is also able to understand the ways and techniques developed for the manufacturing of an object.

When an artefact with colored surface must be investigated like wall paintings, XRF analysis can provide a lot of useful information about the pigments used for the decoration or construction. When it comes to pigments used in roman times, their analysis should not be very difficult if it is considered that their numbers are limited and their composition is published (Chiari and Scott 2004). However this method cannot characterize pigments but can only refer to the elements which compose it, so pigments with similar elemental compositions cannot be differentiated only through XRF (McGlinchey, 2012). XRF is a good tool for the examination of painted works of art and archaeological objects and the identification of elements characteristic of

pigments (McGlinchey, 2012) and especially on wall paintings a characterization of the pigments can be possible, if combined with the observed color or records of the pigments commonly used at a certain period.

Knowing the chemical composition of pigments, XRF can identify the materials used, but the analysis of objects where a layered structure of different and heterogeneous materials is present together with a medium or an organic binder can be rather difficult (McGlinchey, 2012). A wall - painting's structure, preparation layer, paint thickness, and pigment heterogeneity will influence the XRF analytical signal. The stratigraphic nature of paintings is one of the major reasons why data from XRF measurements will prohibit quantitative analysis and the results taken from such an object can even be deceptive qualitative (Shugar and Mass 2012). Because of the penetrating nature of the X-rays, information from a layered structure will be taken by all layers simultaneously. Elements detected from lower layers of the object can be either attenuated or not detected at all due to the absorption of both the incoming and the emitted X-rays through the object. The problem with this phenomenon is that since we are talking about paint layers, it is not expected for the layers to be even everywhere and even the attenuated elements to produce a uniform reduction.

The different thickness of the paint layers can cause many problems to their identification so the best approach is to take measurements from multiple areas of the object where the same pigment appears to be. The strongest signal of an element can guide the researcher to understand the main composition of a certain pigment (McGlinchey, 2012).

3.6   The roman sites of Villa del Casale and Benedictine Monastery of San Nicolò l'Arena

The roman Villa Del Casale is located near Piazza Armerina commune in the province of Enna in Sicily, southern Italy and it is dated around 4th and 5th century A.D. It is spread out along three great terraces at the foot of a hill on the road connecting the cities of Catania and Agrigento. Its building was ordered by an eminent member of the Roman Senatorial aristocracy. Based on stratigraphic and historical data, and literary sources, the dating of the Villa is fixed as not later than 340 A.D. (Pensabene and Gallocchio 2011). The Villa is known for its very well preserved roman mosaics, but big interest is focused on the fresco wall - paintings in almost every room of the

villa. The most extraordinary about the wall paintings of the villa is that they cover not only the interior of the rooms' walls but also the exteriors. The first excavation of the Villa is dated to the 1950s and since then several have carried out by archaeologists with the last one still going from 2004 (Pensabene and Gallocchio 2011).

The Benedictine Monastery of San Nicolò l'Arena is located in the historical center of Catania city with the church of San Nicolò l'Arena. In 1977 the Monastery was donated to the University of Catania by the Municipality that used it for the Faculty of Humanities. It is dated in the 16th century and its construction continues until today. It was founded by a Cassinese congregation in 1558. The modification of the original structure was defined by two natural phenomena, the lava eruption of Etna in 1669 A.D. and the earthquake of 1693 A.D. Various modifications and reconstructions have carried out through the centuries. More recently in 1984 A.D., the restoration and conservation of the monastery took place, that lasted thirty years and has led to the discovery of the history of the town from the Roman period to the present day (Ippolito, 2017). An entire Roman neighborhood with the two main axes the Cardum and the Decumanus Maximus, houses of the Hellenistic (323- 31 B.C.) and imperial time has been found under the monastery. In particular, a roman house (domus) decorated with wall paintings and its court (peristilio) is still visible within the university library, perfectly integrated in the structure of the 16th century monastery. (Monastero dei Benedettini, Catania www.monasterodeibenedettini.it)

4 Materials and Methods

Seven (7) Roman wall painting fragments were analyzed by means of a 3D micro-XRF spectrometer. The four (4) fragments derive from the roman Villa Del Casale in Piazza Armerina and another three (3) from the Roman house of the Benedictine Monastery of San Nicolò l'Arena in Catania. The fragments studied are all stored in Laboratory of Non-Destructive Analysis in situ (LANDIS) embedded in the National Institute for Nuclear Physics (INFN) in Catania. Many more fragments from the same Roman sites were available but an emphasis was given to the ones that appear a stratigraphy of two or more paint layers with a calcium-based preparation. All of the fragments were constructed with the method of buon fresco[2]. The finds were analyzed with the 3D micro-XRF spectrometer by performing 1D (depth), 2D (area) and 3D (volume) measurements to identify the inorganic pigments used, to distinguish the paint stratigraphy and possibly to quantify the thickness of each individual layer

For the characterization of the 3D micro XRF set-up of the, eighteen (18) mono-elemental and compound Micro-Matter targets provided by LANDIS were also measured.

---

[2] Buon fresco is the Italian term for true fresco in which alkaline-resistant pigments, ground in water, are applied to wet plaster. The pigments are applied on the wet plaster as soon as it is applied on the wall, so when it is dried the pigments become one with the plaster.

4.1   Standard materials

Eighteen (18) single-element or compound Micro-Matter targets (*Figure 3*) were measured to determine the energy calibration and resolution of the X-ray detector, the in-depth spatial resolution nd the elemental sensitivity of the confocal micro-XRF set-up . The measured targets were Ti, V, Cr, Mn, Fe, Co (3 μm)[3], Ni (2 μm), Ni (6 μm), Cu, Cu (8 μm), Cu (bulk), Ge, CsBr, ZnTe, RbI, Sn and Pb.

Figure 3 Micro Matter targets

---

[3] Co (3 μm), Ni (2 μm), Ni (6 μm), Cu (8 μm), Cu (bulk) are thicker foils and each number represents each target's thickness.

4.2 Wall-painting samples

In this section the wall – painting samples from both roman sites are introduced and their characteristics are presented.

AFF16 (VC17) (*Figure 4*)

This sample comes from the roman house located in the Benedictine Monastery of San Nicolò l'Arena in Catania. It is about a small fragment of wall – painting of about 2 x 2 cm dimensions and thickness 0.5 cm. It is painted half red and half green, in which the red part of the wall painting is the top layer and covers in some areas the green layer. Below the color layers is visible a white preparation layer and under that a more

Figure 4 Aff16 wall - painting fragment

coarse and thick layer than the upper ones. The fragment is in good preservation state. Individual abrasions appear in the whole surface of the fragment as well as some discoloration especially in the green area. Deposits of dust cover the whole surface.

A8 (*Figure 5*)

This sample is originated from Villa Del Casale in Piazza Armerina. Its dimensions are around 4 x 2 cm and thickness around 1 cm. A white area covers most of the surface of the wall – painting fragment. It is not clear if that area is also the preparation layer of the wall – painting. A red – yellow layer that seems like a brushstroke, covers the white color area at the edge of the fragment. Under all the pre-mentioned layers there is a coarser and thicker one that contains big inclusions. The fragment is in very good preservation condition. A few abrasions appear in the yellow color layer and the white color
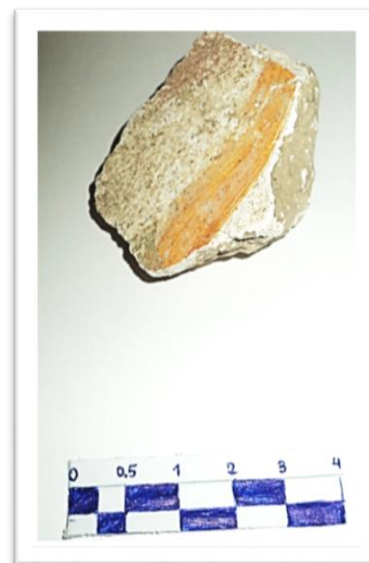
Figure 5 A8 wall - painting fragment

area. A thin layer of dust/soil covers the whole surface.

Sample 1 (*Figure 6*)

This sample was untitled and non-categorized so it was named Sample 1. It is a large wall – painting fragment of about 18 x 13 cm wide and thickness 2 to 3 cm. The fragment is originated from Villa Del Casale in Piazza Armerina. The fragment appears a stratigraphy that consists of a white preparation layer covered in parts by three different colors, a light blue, a red and a yellow. Two white parallel stripes appear in the middle of the fragment and limit the blue area between them. The blue area covers the yellow one in some parts. Under the preparation layer, a much coarser one with big inclusions exists. The fragment is in good preservation state.

Figure 6 Sample 1 wall – painting fragment

A network of cracks appear in the color layers of the fragment as well as some discoloration in some parts. Multiple abrasions and loss of color appear in the whole surface of the fragment.

#48 (*Figure 7*)

This sample is also a large wall – painting fragment of about 16,8 x 20,3 cm wide and thickness 2 to 3 cm. The fragment comes from Villa Del Casale in Piazza Armerina. The painted surface is divided in three sections, a narrow white section, a wide yellow one and ends with a narrow dark red section. The dark red layer seems to be the top one and covers a part of the yellow area that covers the white one. It is not clear if the white area is a color layer or the preparation layer that was used in the manufacturing of the wall – painting. A light green drawing starts from the dark red area and crosses over the yellow where it ends. Possibly it is a part
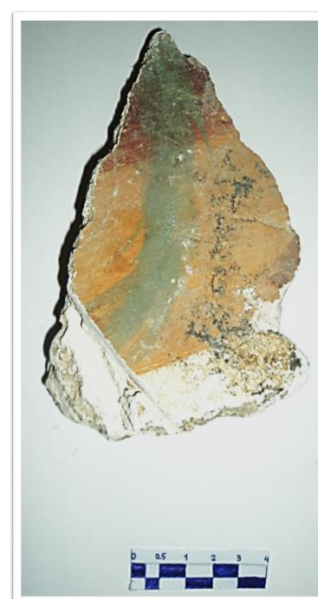
Figure 7 #48 wall - painting fragment

of an herbal theme. A preparation layer is visible under the painted surface. Under the preparation layer there are several layers that get coarser with bigger inclusions. The fragment is in good preservation state. Several small abrasions spread all over the painted surface. A network of cracks appear in the painted layers. Dark stains or deposits are visible in a big part of the surface. All the surface is covered by a thin layer of white dust.

#57 (*Figure 8*)

This wall – painting fragment comes from Villa Del Casale in Piazza Armerina. Its dimensions are 3,5 x 3 cm wide and thickness 0.7 cm approximately. The paint surface is divided in two section, a white one and red one. The white section seems to be the same as the preparation layer and the red layer appears to be on top of that. More layers are distinguishable under the preparation layer. The further the layers are from the painted surface, the coarser they seem. This fragment is also in a very good condition. The red area appears to

Figure 8 #57 wall - painting fragment

have small abrasions, discoloration and in some parts loss of the painted layer. The white area seems more damaged with bigger abrasions. The painted surface is covered by white powder.

AFF4 (BN10) (*Figure 9*)

This sample is originated from the roman house located in the Benedictine Monastery of San Nicolò l'Arena in Catania. Its dimensions are 3 x 4 cm approximately and thickness around 1 cm in one side and getting thinner on the other. The painted surface is covered by a purple color layer. On the edge of the fragment a white thin brushstroke is visible on top of the purple layer. A white preparation layer is visible under the purple layer. Several layers that seem coarser constitute the substrate of the wall painting. The fragment is in

Figure 9 Aff4 wall - painting fragment

good preservation state. The purple surface appears to have some small abrasions and loss of the painted layer. A white transparent pattern like tentacles on one side of the fragment indicates the presence of salts once solute and now solid, most probably due to humidity. The whole surface was covered by deposits of white powder.

AFF2 (BN9) (*Figure 10*)

This sample also comes from the roman house located in the Benedictine Monastery of San Nicolò l'Arena in Catania. It is 2,8 x 2,5 cm wide and 0,5 cm thick. A red color layer covers the biggest part of the painted surface, while on one edge a second darker (black or blue) layer is visible. The darker layer seems to be on top of the red one. Under the painted surface a white preparation is visible. Coarser layers constitute the rest of the wall painting substrate. There are many abrasions scattered all over the painted surface as well as loss of the painted layer especially in the area where the two different paint layers meet. The whole surface is covered by a thin layer of white powder.

Figure 10 Aff2 wall – painting fragment

4.3 The LANDIS 3D Micro-XRF spectrometer

The 3D Micro-XRF measurements were performed at the LANDIS laboratory of INFN, in Catania, Italy. (*Figure 11*). The target material of the anode of the X-ray tube (by IFG) is Molybdenum (Mo). The tube operational voltage was set equal to 50 kV.. The exciting X-ray beam is focused at spot size within the micrometer regime by means of a polycapillary X-ray lens (by IFG). The angle of the incoming and outgoing beam with respect to the sample surface was set equal to 45˚. For the detection of characteristic X-rays, two silicon drift detectors (SDDs by Ketek) are employed, the one placed within the horizontal plane (h-SDD), whereas the other is set inclined at 45 degrees with respect to the horizontal plane (i-SDD). The h-SDD is coupled with a polycapillary half lens (by IFG) to allow confocal micro-XRF measurements. The data acquisition and signal processing by the two SDDs is handled by two respective Digital X-ray Processors (DXP by Brightspec). The 3D micro-XRF system is also equipped with an optical microscope (by Infinity) which is used for positioning the sample at the optics focal distance, where beam-spot is minimal, but also for acquiring high resolution images of tiny areas of the sample.

Figure 11 The LANDIS 3D Micro - XRF spectrometer

4.4 Data analysis and software tools

The spectra acquired by the measurement of each sample, whether a wall – painting fragment or Micro-Matter target, were processed through several software tools. For the evaluation of the spectra, the PyMCA 5.4.0 software and ROI imaging tool (PyMCA's tool) were used. The depth elemental profiles, were created through the combination of two different software, ImageJ 1.52a and OriginPro 2016 (64 – bit). Elemental correlations obtained from the 2D measurements were processed by means of the XRF Imaging Rev software developed in-house by LANDIS at INFN. Finally, for the creation of the 3D imaging models of the wall – painting paint layer stratigraphy, the Icy 1.9.9.1 software was used.

4.5 Analytical methodology

Depending on the paint-layer stratigraphy and its preservation state,   specific type of measurements were carried out according to the information displayed in *Table 1*.

Table 1 XRF applications

Sample	Number of spots examined		
	Depth analysis (1D)	Areal analysis (2D)	Volume analysis (3D)
AFF16 (VC17)	2	1	1
A8	3	1	-
Sample 1	1	1	-
#48	2	1	-
#57	3	1	1
AFF4 (BN10)	4	1	-
AFF2 (BN9)	4	1	1[4]

The standard Micro Matter targets were examined by means of in-depth (1D) measurements, only.

The details of each measurement are presented in the following sections.

---

[4] The numbers refer to how many each technique was applied.

In-depth (1D) profiling with confocal micro – XRF analysis

This technique was applied in the wall – painting fragments and the Micro-Matter targets.

The in-depth (1D) measurements of the Roman wall – painting samples were performed with a 5 μm step up to a depth of 200 to 250 μm depending on the sample. The time for each measurement was 25 s. In Aff4 sample the time per measurement was 40 s.

In the case of the Micro-Matter targets measured, from the deduced scatter plots of each element characteristic X-ray line intensity versus depth, a curve (Gaussian) fitting by OriginPro was performed[5]. Various calculations were made and information like full width at half maximum (FWHM)[6], sensitivity (counts/time/areal density), the σ[7] value and its error as well as the peak area (A) and its error were recorded. The FWHM of all the Micro-Matter targets were plotted together towards their energy.

The scanning parameters of each sample's measurement can be seen in **Table 2**.

After their acquisition, the spectra were processed by ROI imaging tool. A calibration file was created to translate the channels[8] of each peak of the gained spectra to energy. A configuration file was created containing all the specifications of the 3D Micro-XRF instrument. The peaks of each spectra were identified and selected at each configuration file. A standard matrix material was created in the configuration file to represent very approximately the composition of our samples. With ROI Imaging Tool the data of each analyte peak were extracted. Next, using the OriginPro software the in-depth elemental profiles, i.e. scatter plots of the elements' counts towards depth (μm) were created for different elements (Si, K, Ca, Ti, Fe, Zn, As, Hg, Pb).

.

---
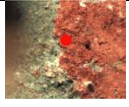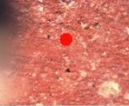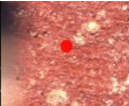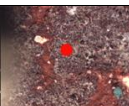
[5] Each scatter plot was fitted by a Gaussian function $y=y\_0+A/(w\cdot\sqrt{(\pi/2)})\cdot e^{\wedge}(-2 \llbracket((x-xc)/w)\rrbracket ^\wedge 2)$.
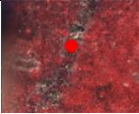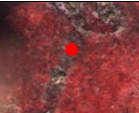
[6] FWHM is the full width at half maximum of the Gaussian profile.

[7] σ expresses the standard deviation.

[8] The DPX analyzer "reads" each electrical signal that the SDD detector provides from each measurement as channels for a certain element. Each channel corresponds to a certain energy.
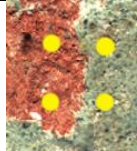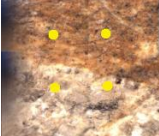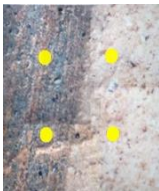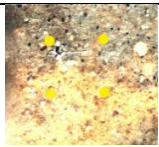
Table 2 In-depth (1D) measurements' parameters
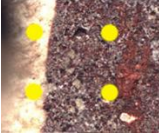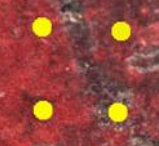
Sample	Area	Photo	Step (μm)	Time per measurement (s)	Depth (μm)	Number of measurements
Aff16	Green		5	25	200	40
Aff16	Red		5	25	240	48
A8	Yellow		5	25	200	40
A8	Yellow		5	25	200	40
A8	Yellow		5	25	200	40
Sample 1	Blue		5	25	200	40
#48	Green		5	25	250	50
#48	Green		5	25	250	50
#57	Red		5	25	250	50
#57	Red		5	25	250	50
#57	Red		5	25	250	50
A4	Purple		5	40	250	50
A4	Purple		5	40	250	50

A4	Purple		5	40	250	50
A4	White		5	40	250	50
Aff2	Red		5	25	250	50
Aff2	Red		5	25	250	50
Aff2	Red		5	25	250	50
Aff2	Brown		5	25	250	50
Ti	-	-	5	10	150	30
V	-	-	3	20	150	50
Cr	-	-	3	20	150	50
Mn	-	-	3	20	150	50
Fe	-	-	3	20	150	50
Co	-	-	5	1	100	20
Ni (2 μm)	-	-	3	1	150	50
Ni (6 μm)	-	-	3	1	150	50
Cu	-	-	3	20	150	50
Cu (8 μm)	-	-	3	1	150	50
Cu bulk	-	-	3	1	150	50
ZnTe	-	-	3	20	150	50
Ge	-	-	3	20	150	50
CsBr	-	-	3	20	150	50
RbI	-	-	3	20	150	50
Sn	-	-	3	20	150	50
Pb	-	-	3	20	150	50

Area (2D) Micro-XRF imaging

This technique was applied only in the wall – painting fragments. The measurements'
parameters can be seen in *Table 3*.

Table 3 2D measurements' parameters

Sample	Photos	Step (µm)	Time per measurement (s)	Area size (mm)	Number of measurements
Aff16		20	1	1 x 1	2500
A8		20	1	1 x 1	2500
Sample 1		20	1	1 x 1	2500
#48		20	1	1 x 1	2500
#57		20	1	1 x 1	2500
Aff4		20	1	1 x 1	2500
Aff2		40	1	0,8 x 0,8	400
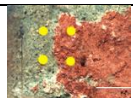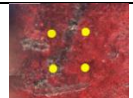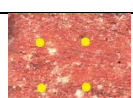
After spectral acquisition the data of each analyte peak were extracted. The counts of each element were examined through the XRF Imaging Rev software to observe the elemental intensity associations between them and identify at which area of each sample a spatial co-existence of these elements appears.

Two regions of interest (ROI) were selected to each sample in their different color areas. The two spectra that were extracted from each sample were compared.

3D imaging with micro – XRF

This technique was applied in only three samples. The three wall – painting fragments are Aff16, Aff2, #57. The scanning parameters are presented in *Table 4*.

Table 4 3D measurements' parameters

Sample	Photo	Step			Time per measurement (s)	Area size	Number of measurements
		X (μm)	Y (μm)	Z (μm)			
Aff16		20	20	10	8	0,4 x 0,4 x 0,15	6.000
Aff2		40	40	5	3	0,8 x 0,8 x 0,25	20.000
#57		20	20	5	3	0,4 x 0,4 x 0,2	16.000

The procedure that was followed for the creation of the calibration and configuration files was the same as in the two previous techniques for the measurement of the wall – painting fragments.

A ROI was selected for the major elements Fe, Ca, and Hg of the samples. The images of all the ROIs from every different depth scans (Z scan) were collected and saved in .tif form. After their extraction, the .tif files from every depth were inserted in ImageJ software and merged all together for every different element. The merged file, which was emerged from this procedure, was inserted in Icy software and visualized into a 3D model. More than one elements could be 3D visualized together using different color coding.

5 3D Micro-XRF set-up characterization

The characterization of the XRF system involves the energy calibration of the multichannel analyzers used for processing the data acquired by both SDDs, the determination of the in-depth spatial resolution and of the confocal set-up elemental sensitivity.

5.1 X-ray detectors energy calibration

For the energy calibration the spectra acquired from the measurement of different standard reference materials (single-element or compound Micro-Matter targets) were employed. More analytically, the channel at which the peak that the characteristic X-ray of each element appears within its spectrum is recorded and then using the OriginPro software the channels and respective characteristic X-ray energies are plotted and fitted using a linear fit (*Figure 12*).

Equation	y = a + b*x
Plot	Energy
Weight	No Weighting
Intercept	0.00904
Slope	0.01438
Residual Sum of Sq	2.60542E-4
Pearson's r	1
R-Square(COD)	0.99999
Adj. R-Square	0.99999
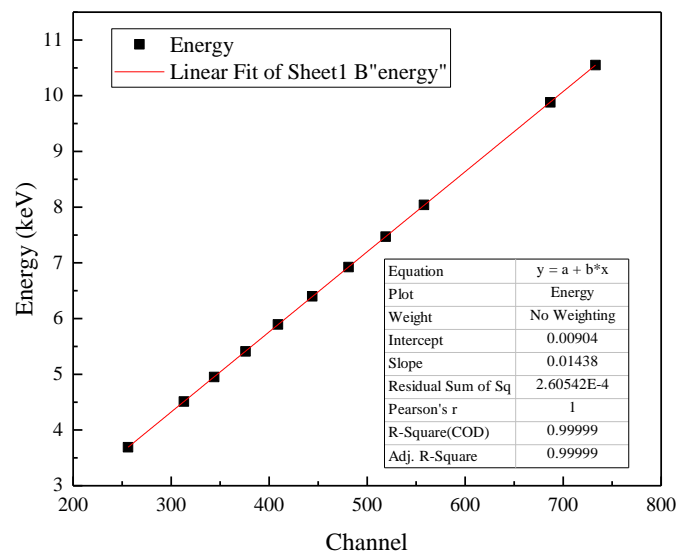
Figure 12 Energy calibration scatter plot of confocal SDD detector

From the linear fitting of the scatter data, the Intercept and Slope are exported and included in the spectrum analysis configuration file

It should be mentioned that each characteristic X-ray line appears in the energy dispersive spectrum with the form of a Gaussian function. The essential features of this distribution are its centroid that reflects the energy of the characteristic X-ray line and the full - width - at - half – maximum (FWHM) (*Figure 13*) that indicates the quality of

the X-ray detector used. (Woldseth 1973). The Gaussian distribution is expressed by the following function:

$$y = y_0 + \frac{A}{2\sigma \cdot \sqrt{\frac{\pi}{2}}} \cdot e^{-2(\frac{x - xc}{2\sigma})^2}$$

where A is the peak area, σ is the standard deviation and xc the peak centroid. The FWHM of each Gaussian distribution is expressed by the function:

$$FWHM = 2\sigma \cdot \sqrt{2ln2}$$
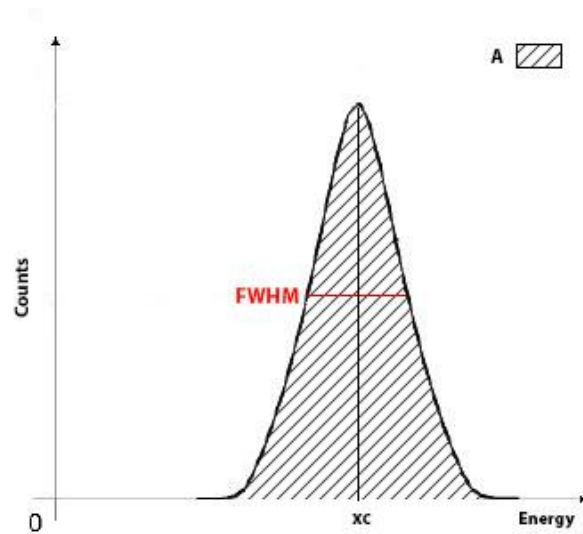
Figure 13 Energy resolution definition in a spectroscopic system

SDDs offer higher performance in term of lower electronic noise at very short peaking times which provides a better and a much better energy resolution at moderate count rates and even at very high – count rates respectively (Caliri, 2017). The energy resolution of an X-ray detector by convention is expressed for Mn-Kα and it was found for the confocal SDD to be equal to 148 eV.

5.2 Spatial resolution

The confocal geometry of the XRF system contains two optics; one of the optics is assigned to the detector and one to the excitation beam. A probing volume in micrometric scale is created when the focus of the detector's optic and the focus of the excitation optic of the microprobe intersecting each other. With moving the object through this probing volume in micrometric steps, the intensity profiles of the elements towards the position of the object can be obtained that will result in information about

the in-depth resolution. The combination of this technique with the 2D imaging technique of the XRF can result in a 3D spatial resolution.
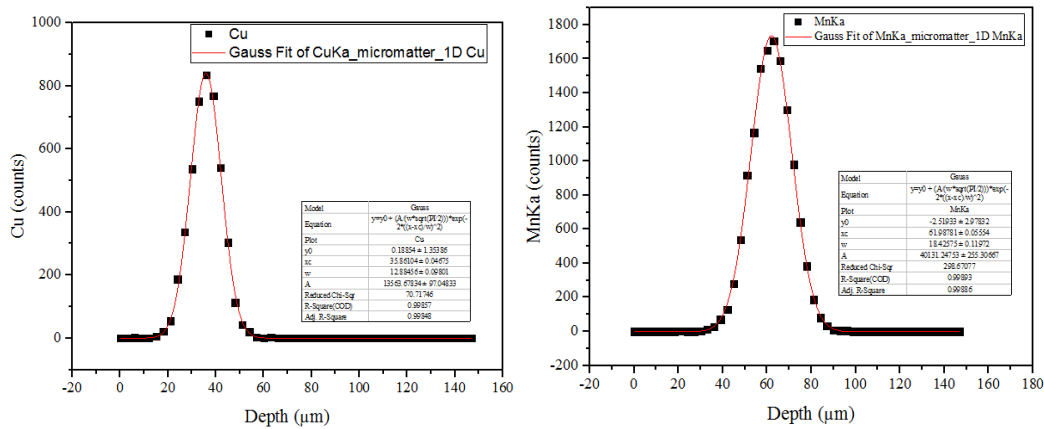
Figure 14 Micro matter targets, depth resolution CuKa (left) and MnKa (right)

To specify the spatial resolution of the confocal SDD detector that was used, the FWHM of all the micro matter targets were calculated (*Figure 14, Figure 15*).

Because of the nature of the 1D measurement, the scatter plots refer to the depth resolution of the detection system.
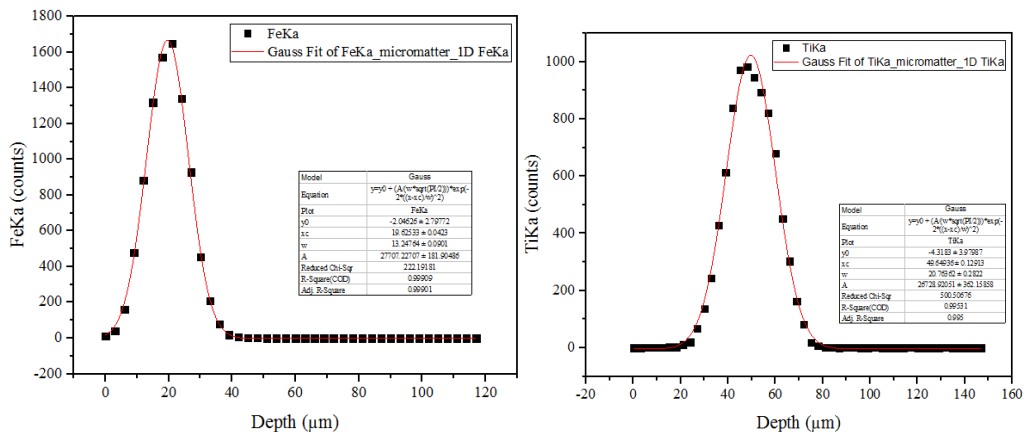
Figure 15 Micro matter targets, depth resolution FeKa (left) and TiKa (right)

The FWHM of the materials were plotted towards their energy as mentioned in section 4.5 (*Figure 16*).
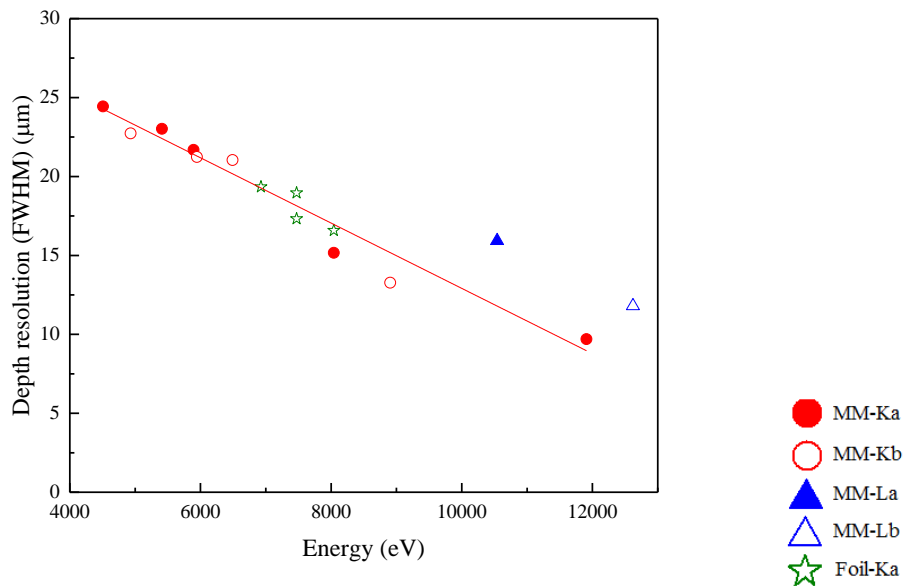
Figure 16 Energy resolution FWHM to energy, where MM-Ka, MM – Kb, MM – La, MM – Lb and Foil - Ka the FWHM of the Ka, Kb, La, Lb and Ka (of foils) of micro matter peaks respectively

In the scatter plot it is clear that the resolution decreases when the energy gets higher. The MM – La and MM – Lb appear to be experimental errors of the analysis.

5.3 Elemental sensitivities

An important part of the set up characterization of the XRF system is the efficiency of the detector. For the determination of the detector efficiency the elemental sensitivities of the micro matter targets were extracted and plotted towards their energies (*Figure 17*). The elemental sensitivities were extracted by the following function:

$$Elemental\ sensitivity = \frac{A}{t \cdot \xi}$$

where A is the peak area (counts), t the time (s) and ξ the elemental areal density ($\mu g/cm^2$).
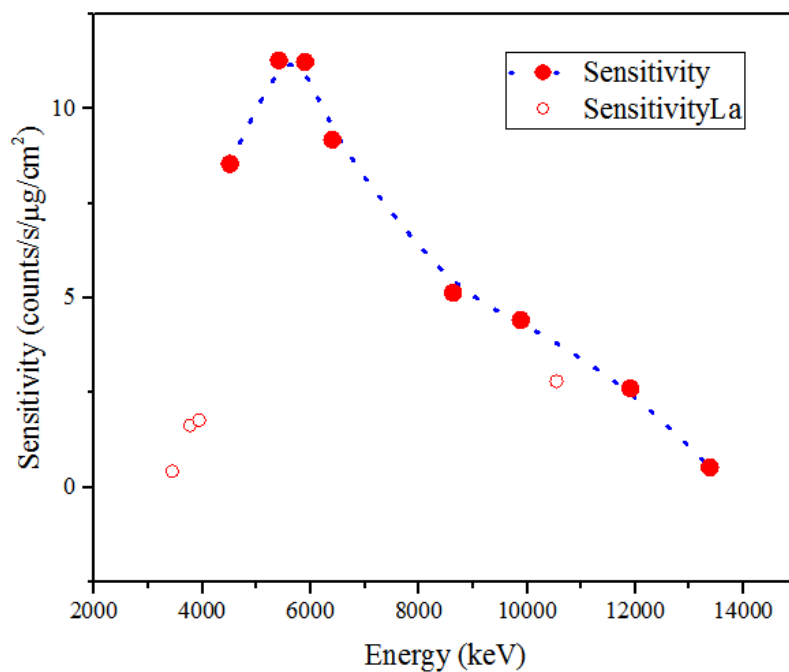
Figure 17 Detector's efficiency via elemental sensitivities of micro matter targets

In the plot it is clear that there is an increasing of the tendency where it creates a peak and after that it starts decreasing. That shows that the detection system of the XRF is more sensitive in detecting certain elements (Cr, Mn) and as the energy increases the sensitivity of the system to detect elements of higher atomic number decreases.

Not a lot of measurements were available for the sensitivities of the La peaks to create a meaningful tendency.

6 Results

6.1 Composition of Roman pigments

In all the samples an area was chosen where the 2D measurement was taken. All the 1D measurements were taken within the mentioned area. On the samples that 3D measurements were applied, the chosen areas match the one in 2D measurement.

From the Areal (2D) measurement spectra, the pigments of the samples were identified. The calcium in the spectra of the Roman wall – painting fragments show the presence of probably lime ($CaCO_3$) as a preparation layer. As described by Vitruvius, in the art of fresco, in roman times, the wall was coated by a fresh layer of lime ($CaCO_3$) (Duran *et al.*, 2010) and sand (quartz = SiO_2) which also explains the presence of Si in all spectra (Garofano, Robador and Duran, 2014). Also, in the art of fresco the pigments used to be dissolved either in water or in a saturated aqueous solution of lime for their application in the damp lime plaster (Balandier *et al.*, 2017).

The iron (Fe) in some fragments indicate the presence of ochre pigment especially if it combined with the observable color. Ochres contain octahedral iron oxides, hematite (Fe_2O_3) and goethite (FeOOH), the color yellow derives when the goethite is the main iron oxide, while the red color derives when hematite is (Elias et al. 2006).

However, sometimes the color does not indicate the use of either yellow ochre (goethite) or red ochre (hematite) or even a mixture of these two (Elias *et al.*, 2006). Bibliography let us know that Romans use a treatment to heat hematite for the creation of a reddish purple hue (Siddall, 2006).

Apart iron oxides, ochres contain also white pigments like alumino-silicate as kaolinite ($Al_2Si_2O_5(OH)_4$) and illite ($(K,H_3O)(Al)_2(Si,Al)_4O_{10}[(OH)_2,H_2O]$), quartz and calcium compounds like calcite ($CaCO_4$) (Elias *et al.*, 2006). Calcium compounds are present in all ochres. Calcite is the most common calcium compound but gypsum ($CaSO4·2H2O$) is also very common especially in Italian ochres (Elias *et al.*, 2006).

Many counts of K can be assigned to the "green earth" pigment which is characterized as the most frequent green pigment used in roman wall – paintings (Garofano *et al.*, 2011). Green earth pigment contains types of clay micas celadonite ($K(Mg,Fe,Al)_2(Si,Al)_4O_{10}(OH)_2$) and/or glauconite[9] ($K(Fe,Al)_2(Si,Al)_4O_{10}(OH)_2$)

---

[9] Celadonite and glauconite have similar compositions but are formed under different geological conditions. Both are found as grey – green or bluish masses and create the same color (Perez-Rodriguez *et al.*, 2015).

(Perez-Rodriguez *et al.*, 2015), so Al, Si and Fe can also be assigned to this pigment. It was not able to distinguish between celadonite and glauconite since the XRF can detect only elements and not compounds.

The copper (Cu) seen in the Sample 1 spectrum is assigned to the light green-blue pigment. Copper is the basis of two green pigments used frequently in Roman wall – paintings, malachite ($Cu_2CO_3 (OH)_2$) and verdigris ($Cu (CH_3COO)_2[Cu (OH)_2]_32H2O$) which is caused by the corrosion of Cu in acidic environment (Debastiani *et al.*, 2016).

The blue pigment azurite($Cu_3 (CO_3)_2(OH)_2$), common in Roman times (Siddall, 2006) contains also copper and since the XRF cannot identify compounds but only elements, it is not certain which of the pigments mentioned was actually used for the creation of the light green-blue in the wall – painting.

The fact that the light green color of the pigment is caused by the use of Egyptian blue ($CaOCuO (SiO_2)_4$) (also common in Roman times) (Siddall, 2006) was rejected. Low counts of Si indicate that it comes from the sand (quartz = SiO_2) used in the preparation of the wall – painting and not due to the existence of Egyptian blue in the wall - painting. Counts of Hg and S in a wall – painting fragment are assigned to the pigment of cinnabar (HgS) (Garofano *et al.*, 2011). Cinnabar was known as a precious pigment that was used frequently in the creation of wall – paintings in the roman times (Bakiler *et al.*, 2016). Cinnabar was made by grinding HgS crystals (gleba) and was mined mainly from Tuscany, Istria and Spain (Aliatis *et al.*, 2010). It was used to be distributed from Rome all over Italy with the expenses of the Villas' proprietors (Bakiler *et al.*, 2016). Cinnabar is observed to be mixed with hematite for the extension of the pigment and to add more brightness to the pigment (Siddall, 2006). In a fragment containing cinnabar the S is certain to derive from there, apart other sources.

The XRF system is more sensitive in detecting Sr which exists inside the mortar of the sample and although it is not in abundance, this is the reason why it appears having so many counts in all samples.

6.2 Scanning micro XRF analysis results

The results from the scanning micro XRF analysis are presented below for each sample.

The spectra were extracted from the ROI taken from the different color areas of each sample. The abundant elements of each paint layer are presented through the differences of the peaks.

An escape peak of CaKa is created at 3,7 keV. The large intensity of CaKa+CaKa creates pile up peak at 7,38 keV energy while the large intensities of FeKa+FeKa and FeKa+FeKb create pile up peaks at 12,8 and 13,5 keV respectively. When there are large intensities of Fe and Ca together, a pile up peak of CaKa+FeKa is created at 10,1 keV. All the pile up peaks of Fe and Ca are presented in Aff16 spectra.

Wall painting fragments from Piazza Armerina

A8

For the 2D measurement the chosen area was on the interface between the yellow and white layers of the sample (*Figure 18*).
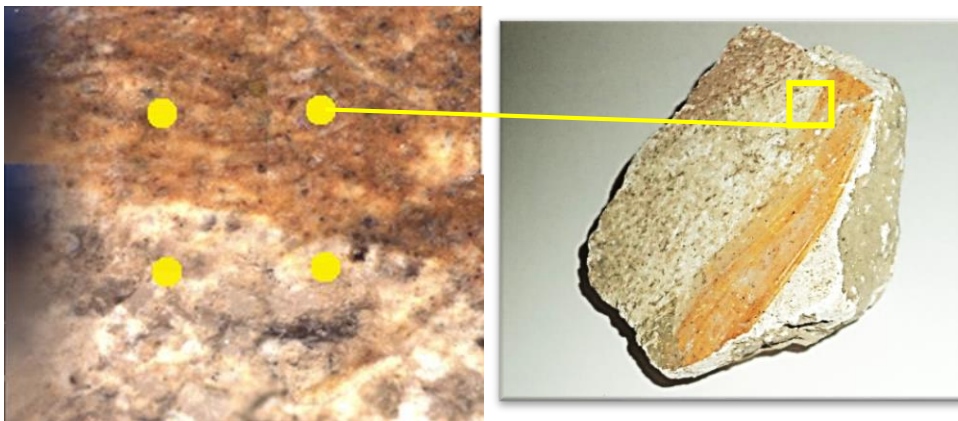
Figure 18 A8 sample microscopic photo 1 x 1 mm of chosen area
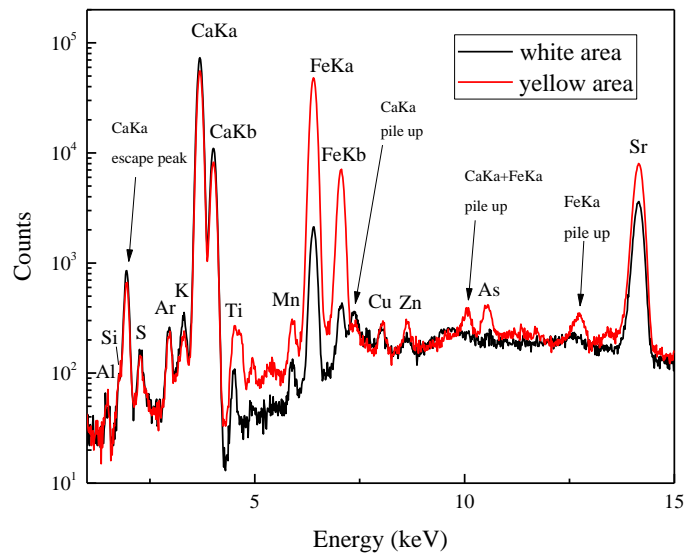
Figure 19 A8 sample, yellow ochre pigment, ROI spectra of the 2D measurement

In A8 sample (*Figure 19*) the Fe peaks extracted from the yellow area show large difference from the Fe peaks coming from the white area. The sample presents high counts of Ca and Fe in the yellow area which are assigned to lime preparation layer and yellow ochre pigment respectively. In the white area of the sample the major elements are also Ca and Fe but the Fe appears in much lower content. The minor elements in the yellow area are Si, S, Ar, K, Ti, Mn, As and Sr.

#48

For this sample the area that was chosen was on the interface between the green and the yellow area (*Figure 20*).
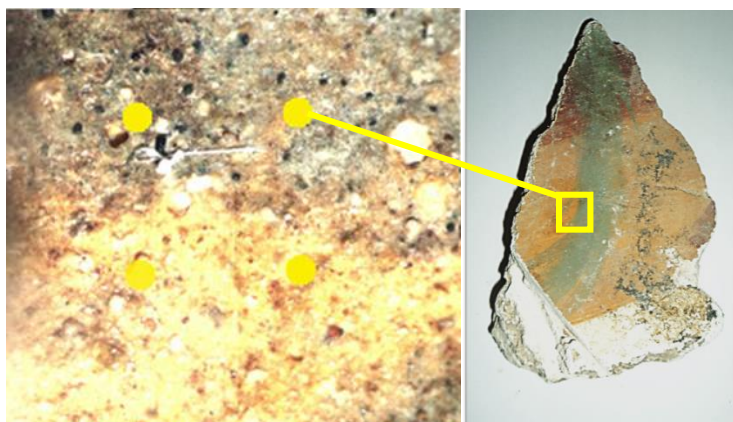
Figure 20 #48 microscopic photo 1 x 1 mm of chosen area
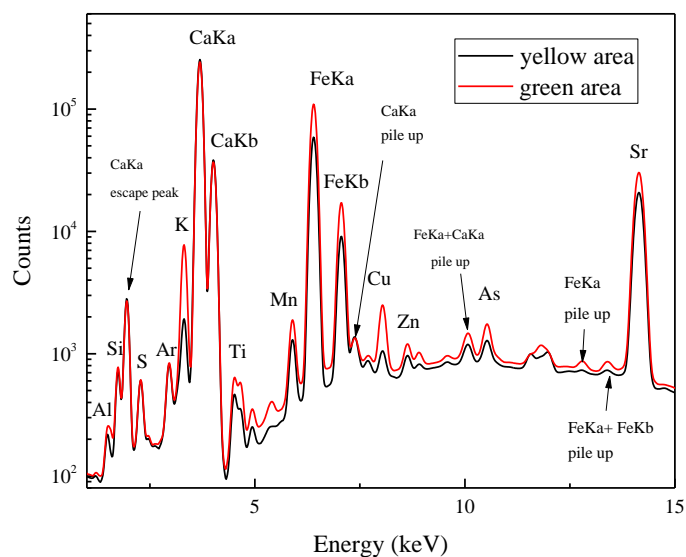
Figure 21 #48 sample, green earth pigment (top layer), yellow ochre (2nd layer), ROI spectra of the 2D measurement

In #48 sample (*Figure 21*) the green area peaks present bigger amounts of Fe, K and Cu than the ones coming from the yellow area. In the green area the major elements in the spectrum are Ca, Fe and K which show the presence of a lime preparation and green earth pigment. In the yellow area the major elements are Ca and Fe. Fe is assigned to yellow ochre pigment. Other elements like Al, Si, S, Ti, Mn, Cu, Zn, As and Sr appear as minor elements in both areas.

Correlations between some elements were observed through the creation of their scatter plots from the 2D measurements and their analysis with XRF Imaging Rev software.
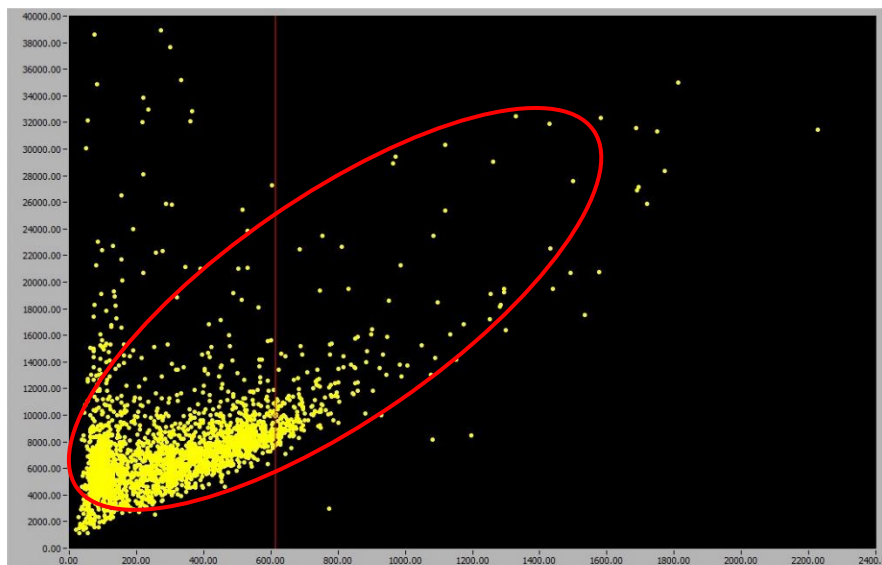
Figure 22 #48 sample, correlation plot between FeKa counts (y axis) and KKa counts (x axis) from 2D measurement

In the scatter plot above (*Figure 22*) a correlation between Fe and K is visible. From the chosen area two images were extracted (*Figure 23*) that show the presence of Fe (left) and K (right) in the sample.
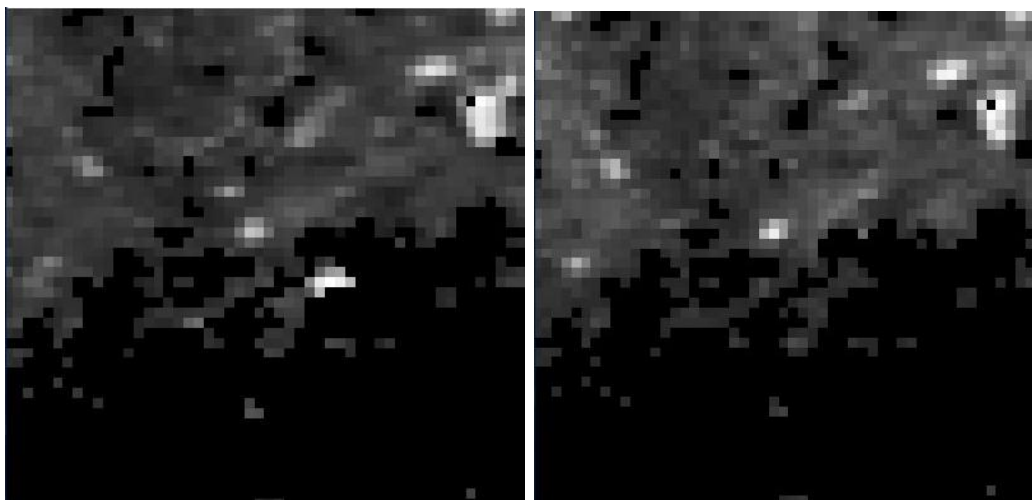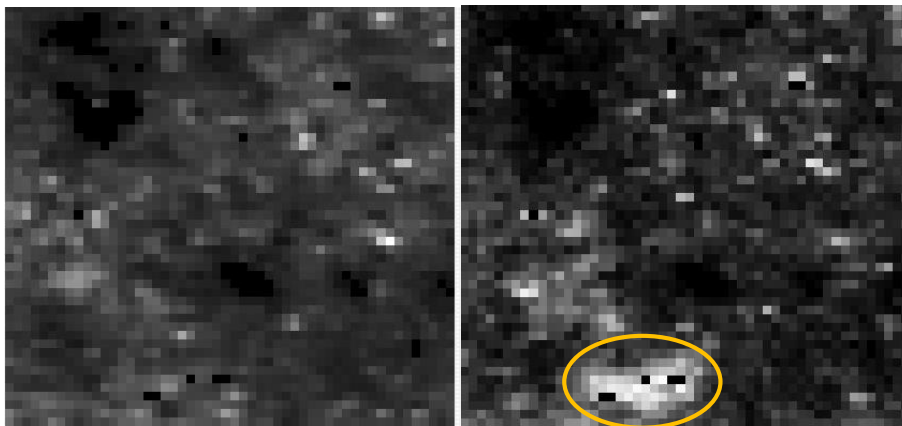

Figure 23 #48 sample, photos of FeKa (left) and KKa (right) from chosen area

The photos reveal that Fe and K are correlated and color dependent in green earth pigment.
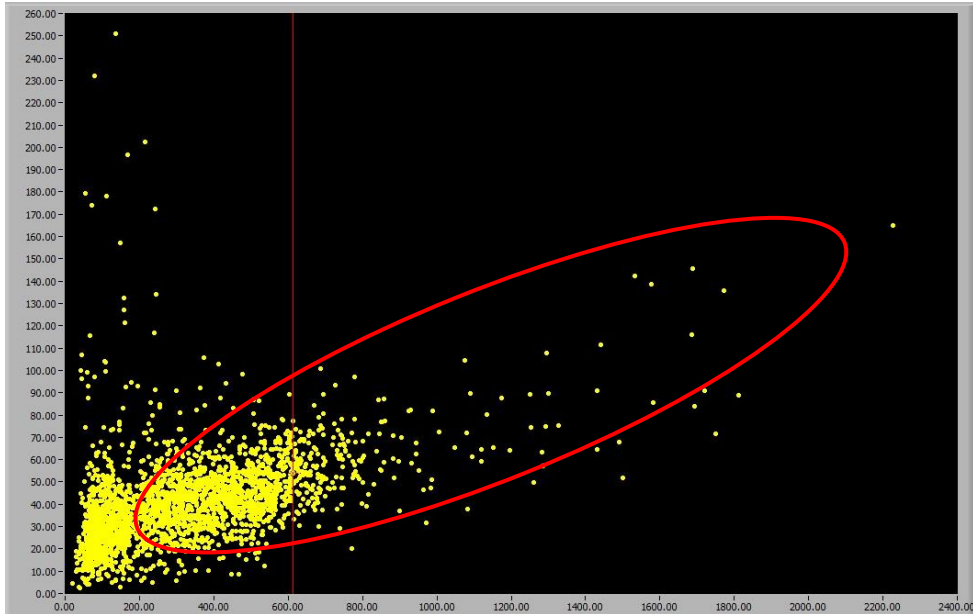
Figure 24 #48 sample, correlation plot between SiK counts (y axis) and KKa counts (x axis) from 2D measurement

In the scatter plot above (*Figure 24*) a correlation between Si and K is visible. From the chosen area two images were extracted (*Figure 25*) that show the presence of Si (left) and K (right) in the sample.
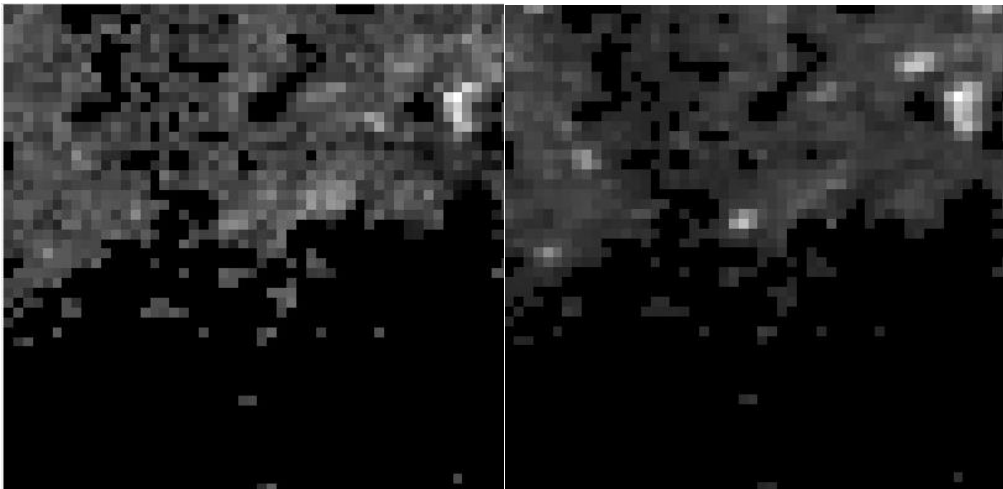
Figure 25 #48 sample, photos of SiK (left) and KKa (right) from chosen area

The photos reveal that Si and K are correlated with green earth pigment.

#57

For the 2D measurement the chosen area was in the red area (*Figure 26*).
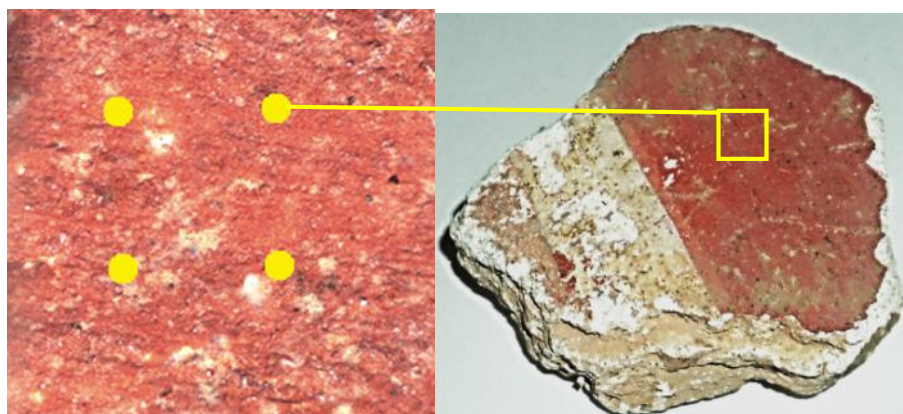
Figure 26 Sample #57 microscopic photo 1 x 1 mm of chosen area
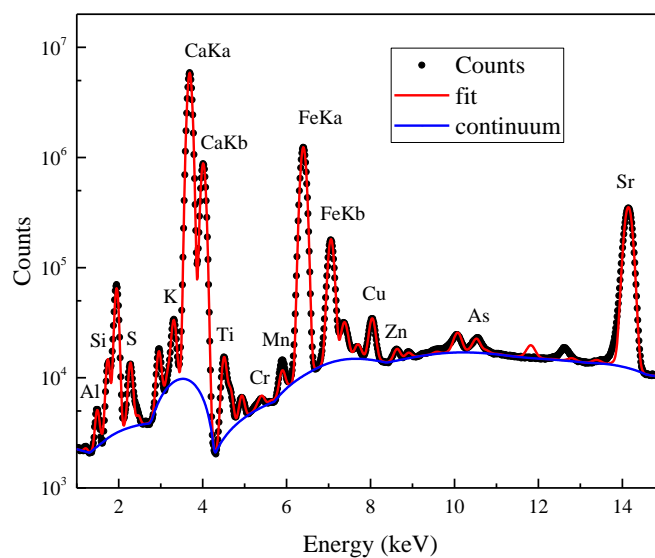
Figure 27 Sample #57, red ochre layer, ROI spectra of the 2D measurement

The #57 sample (*Figure 27*) has not different color areas, so the spectrum comes from the whole 2D measurement. The major elements are Ca and Fe which are assigned to lime preparation and red ochre pigment, respectively. The rest of the elements visible in the spectrum are assigned to minor elements.

Two scatter plots from the 2D measurement were created in XRF Image Rev software, between Fe / Ti and K / Ti that show the relation of the elements in the sample.
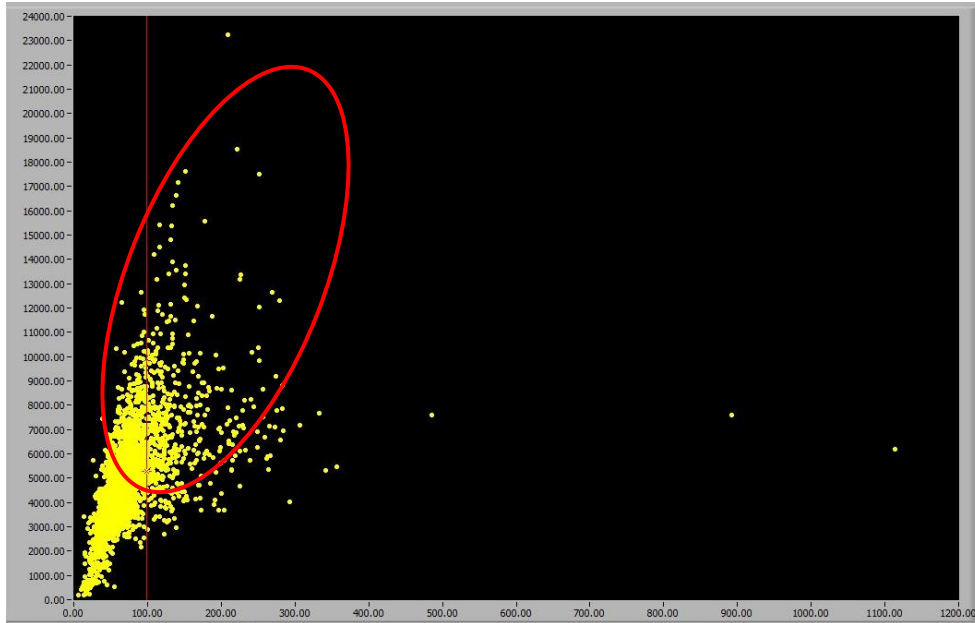
Figure 28 #57 sample, correlation plot between FeKa counts (y axis) and TiK counts (x axis) from 2D measurement

In the scatter plot above (*Figure 28*) a correlation between Fe and Ti is visible. From the chosen area two images were extracted (*Figure 29*) that show the presence of Fe (left) and Ti (right) in the sample.

Figure 29 #57 sample, photos of FeKa (left) and TiK (right) from chosen area, the area marked in the yellow circle indicates the white areas in the original photo of the sample

The photos show that there is not a big correlation of the elements in the color layer. It is interesting to see that the same void areas appear in both images that do not refer to either Fe or Ti. Also in the right photo, Ti seems more intense in the white areas of the original photo of the sample.
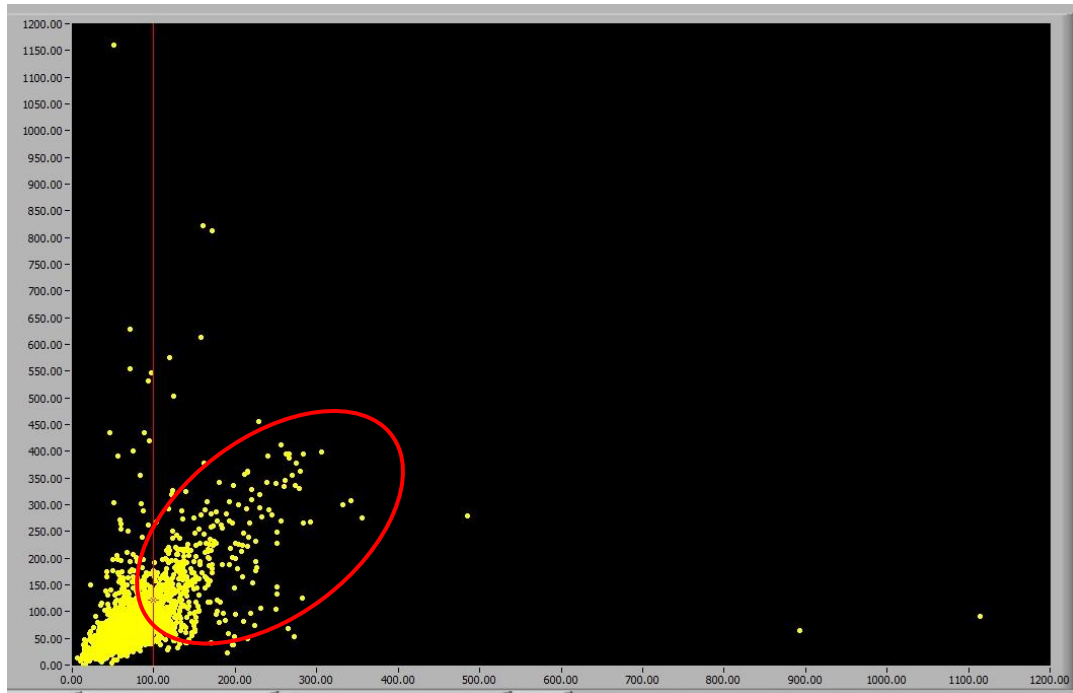
Figure 30 #57 sample, correlation plot between KKa counts (y axis) and TiK counts (x axis) from 2D measurement

In the scatter plot above (*Figure 30*) a correlation between KKa counts and TiK are presented. From the chosen area two images of K and Ti respectively were extracted (*Figure 31*).
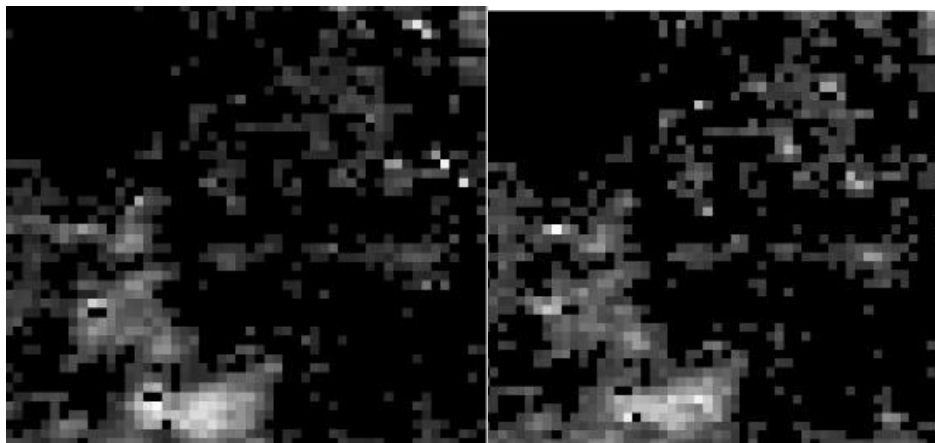
Figure 31 #57 sample, photos of KKa (left) and TiK (right) from chosen area

The photos show a correlation between the two elements, but the statistics of both of them are very low. Since the area that was measured has only one layer of pigment and the preparation, it is not easy to distinguish the dependence of the elements with a certain layer.

In the same area a 3D measurement was also conducted. The major two elements, Fe (green) and Ca (red), were visualized through the use of ImageJ 1.52a and Icy 1.9.9.1 softwares in a three (3) dimension model (*Figure 32*).
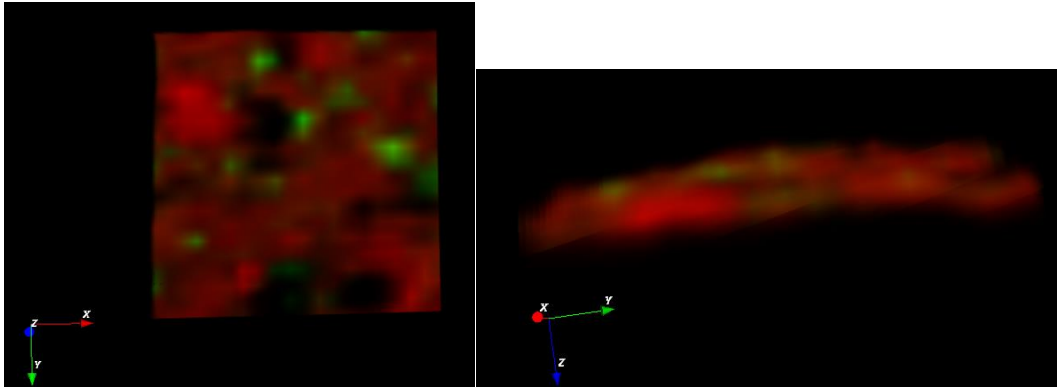
Figure 32 3D model of #57 sample, the color layers are shown from the top (left) and lengthwise (right). Ca is represented with red and Fe with green

In the model Ca seems to be in abundance, which also matches with the 2D spectrum acquired from the same area. Fe in the pictures appears in many areas of the model. Although the Fe (ochre) is on top of the Ca (lime), calcium appears more intense because of its number of counts and that is why iron does not appear like a uniform layer. From the side photo it is visible that iron is on top of the Ca.

The voids in the model match with the white areas in the sample. The void visible in the bottom corner of the model matches with the Ti area found from the photos of the 2D measurement in XRF ImageRev software.

Three different 1D measurements were conducted in this sample all in the red area within the area of the 2D and 3D measurements.

Sample 1

For the 2D measurement the chosen area was between the light green and the white area (*Figure 33*).
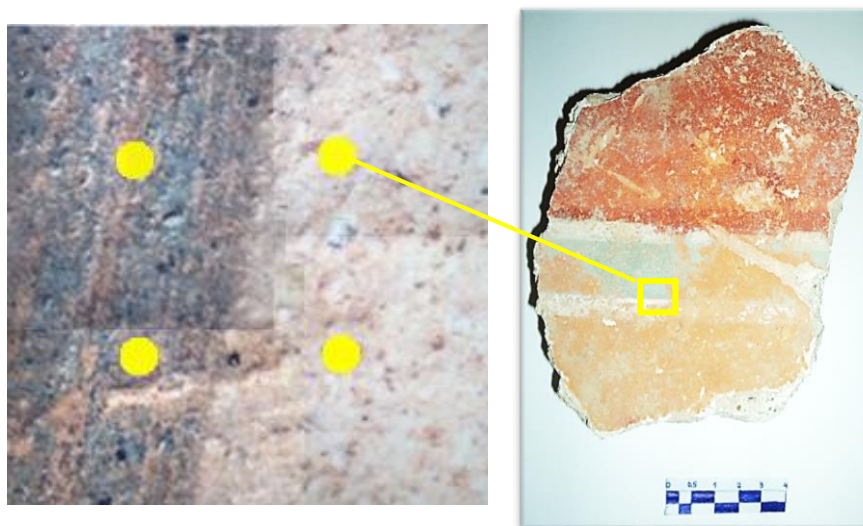


Figure 33 Sample 1 microscopic photo 1 x 1 mm of chosen area
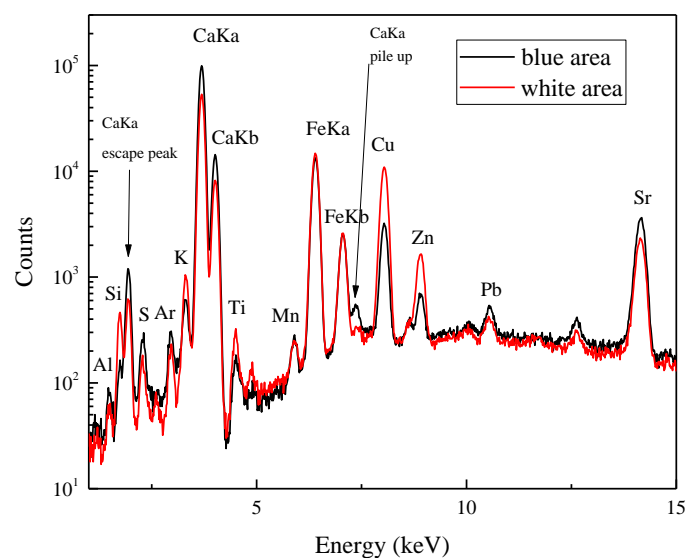
Figure 34 Sample 1, malachite or azurite pigment (top layer), yellow ochre pigment (2nd layer)ROI spectra of the 2D measurement

In Sample 1 (*Figure 34*) the white area appears a bit more abundant in Cu and Zn than the blue area. In the blue-green area the major elements are Ca, Fe and Cu. Ca comes from the lime preparation while Fe comes from the layer of ochre which appears below the

green layer. The Cu in the spectrum is due to the blue-green area which is assigned to either malachite or verdigris or azurite. The white area in the sample presents Ca and Fe as major elements. In this case Fe comes from the ochre pigment layer existing below the top layers. Ca in both spectra comes from the lime preparation layer. The elements Al, Si, S, Ar, K, Ti, Mn, Zn, As and Sr appear as minor elements in both spectra.

Summary of Piazza Armerina's analytical results

From the samples presented above three (3) main pigments were identified, ochre (goethite and/or hematite), green earth (celadonite and/or glauconite) and malachite/verdigris/azurite. As it was mentioned before it was not able to identify which exactly compounds are contained in each pigment.

The preparation layer of all samples is calcium based, probably lime.

In sample #48 iron and silicon show a correlation with potassium in the area where green earth pigment is.

In sample #57 titanium does not appear a particular correlation with any other element but the photos extracted from XRF Imaging Rev software show that Ti appears in the white areas of the sample. In the 3D model that was constructed in the same sample it is not easy to distinguish the different color layers because of the intense of some elements, but the model shows clearly where, elements assigned to certain pigments exist and where they do not in the sample.

Wall painting fragments from Domus Benedectine

AFF16 (VC17)

For the 2D measurement the chosen area was between the green and the red area (*Figure 35*).
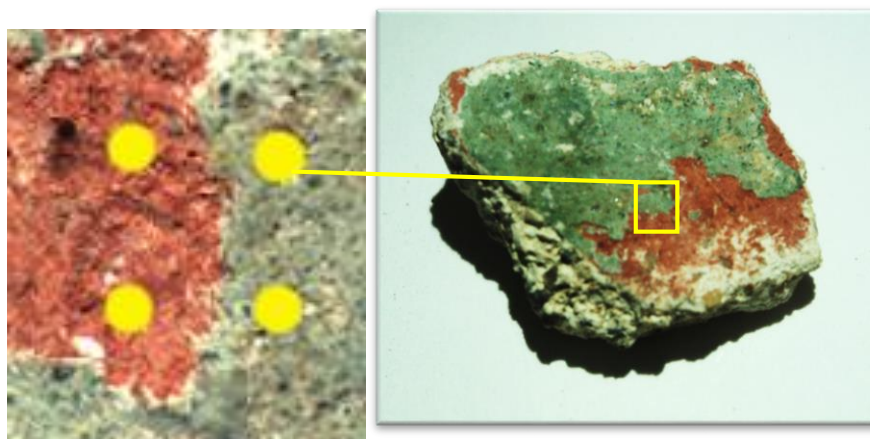
Figure 35 Aff16 microscopic photo 1 x 1 mm of chosen area
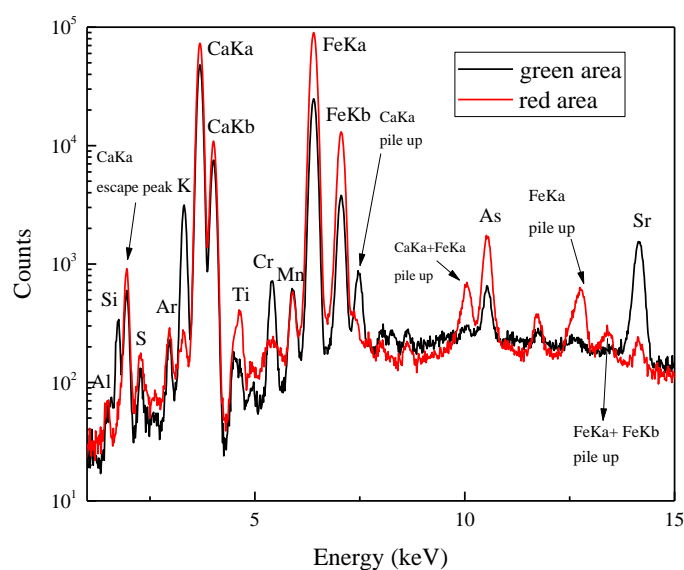
Figure 36 Aff16 sample, green earth pigment (top layer), red ochre pigment (2nd layer), ROI spectra of the 2D measurement

In Aff16 sample (*Figure 36*) differences appear in the peaks of Fe, K and Cu between the colour areas. The red area appears bigger amounts of Fe while the green area shows bigger amounts of K and Cu. The spectrum of the green area presents Ca, Fe and K as

major elements. The presence of high counts of Fe and K in the green area can be assigned to the green earth pigment. In the red area of the fragment the major elements are Ca and Fe. In this area Fe is assigned to red ochre. In both areas Ca is assigned to the lime preparation of the wall paintings. The rest of the elements like Al, Si, S, Ar, K, Ti, Cr, Mn, As and Sr appear in both spectra as minor elements.

From the 2D measurement, scatter plots were created that reveal the correlations of some elements with a certain pigment (*Figure 37*, *Figure 39*, *Figure 41*, *Figure 43*).
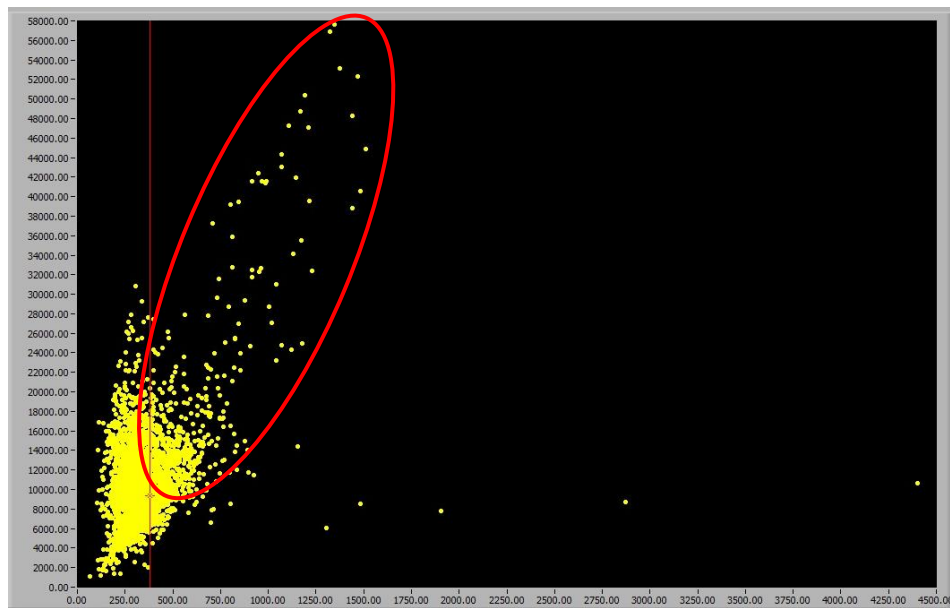
Figure 37 Aff16 sample, correlation plot between FeKa counts (y axis) and AsK counts (x axis) of 2D measurement
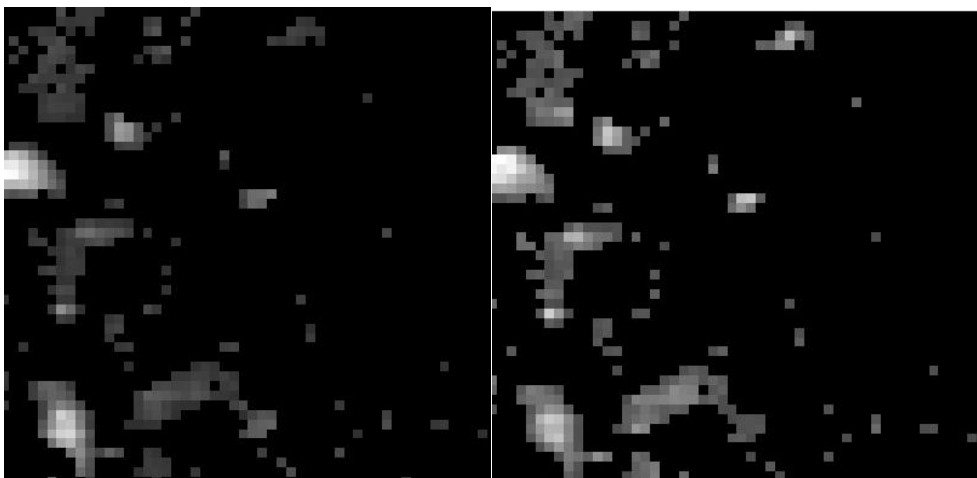
Figure 38 Aff16 sample, photos of FeKa (left) and AsK (right) from the chosen area

From the extracted photos (*Figure 38*) a correlation of the two elements with the area of ochre is visible but the low counts of the As cannot make a clearer image.
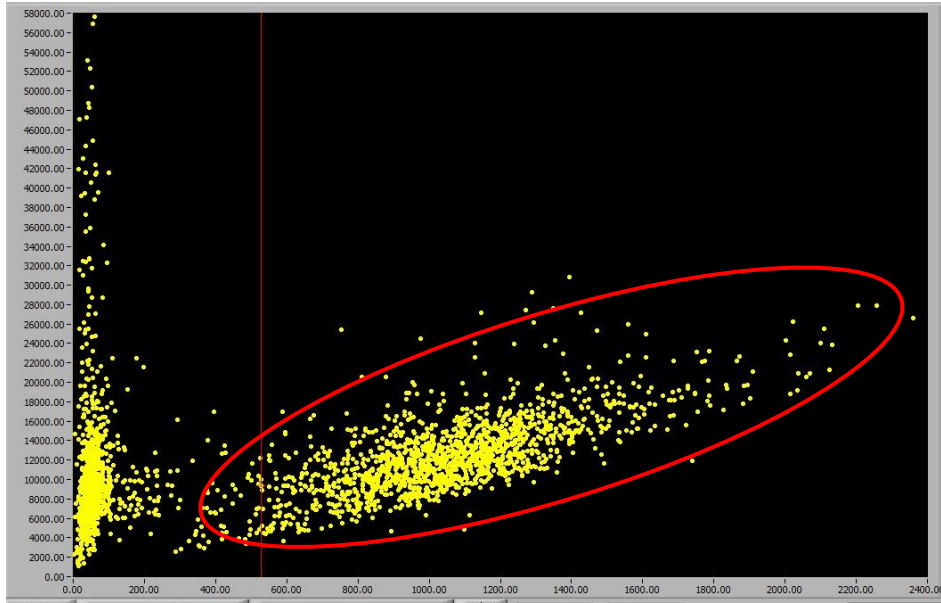
Figure 39 Aff16 sample, correlation plot between FeKa counts (y axis) and KKa counts (x axis) of 2D measurement
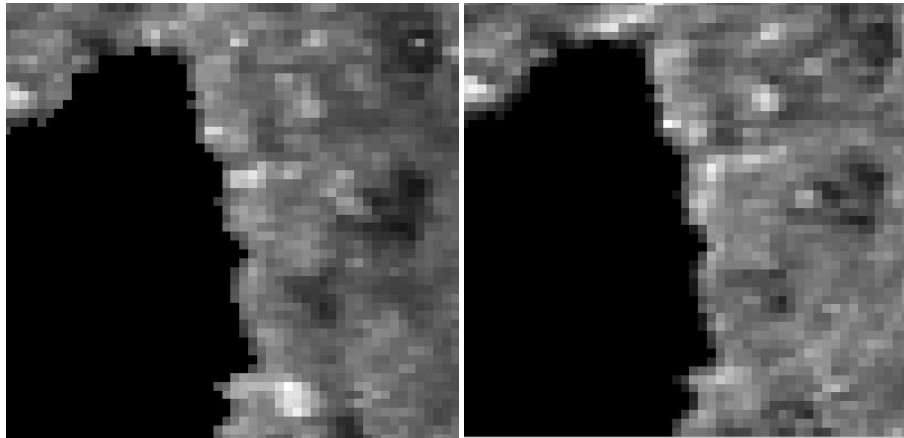
Figure 40 Aff16 sample, photos of FeKa (left) and KKa (right) of chosen area, color correlated of the two elements to the green earth pigment

The photos (*Figure 40*) extracted from the scatter plot of the elements show clear correlation between them. Both of them show a correlation with the pigment of green earth.[10]

---

[10] The correlation of the two elements does not mean that Fe does not exist in the area of ochre also. As seen in the scatter plot, Fe extends also in a different tension upwards where it is not correlated with K which presents the area of ochre.
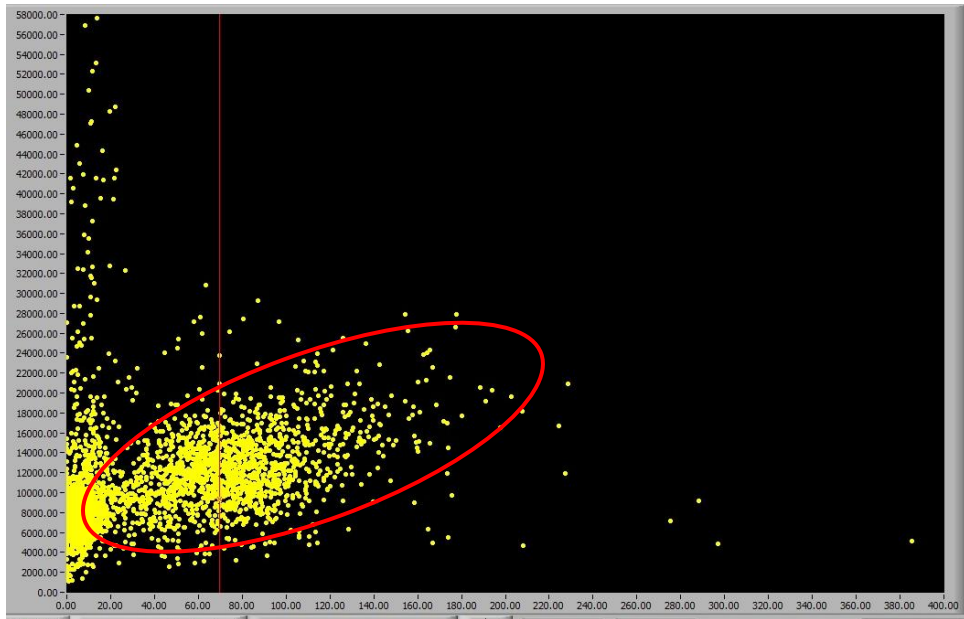
Figure 41 Aff16 sample, correlation plot between FeKa counts (y axis) and SiK counts (x axis) of 2D measurement
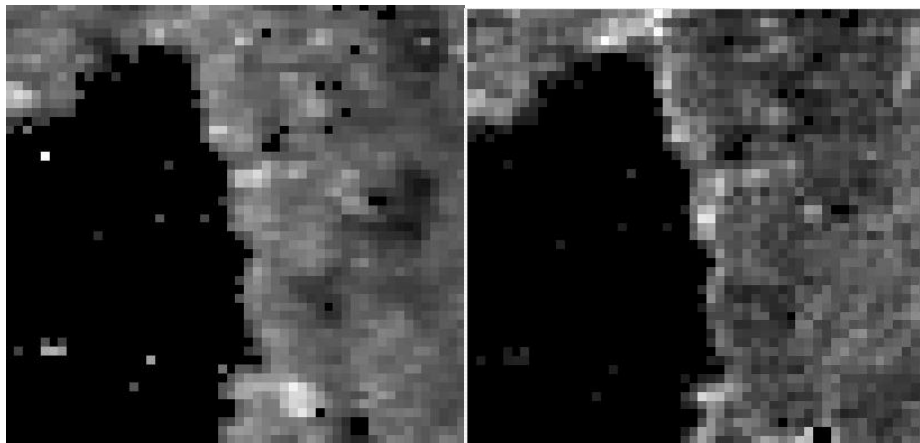
Figure 42 Aff16 sample, photos of FeKa (left) and SiK (right) of chosen area

The photos (*Figure 42*) above show another correlation of Fe and Si with the green earth pigment, despite the bad statistic of the Si.
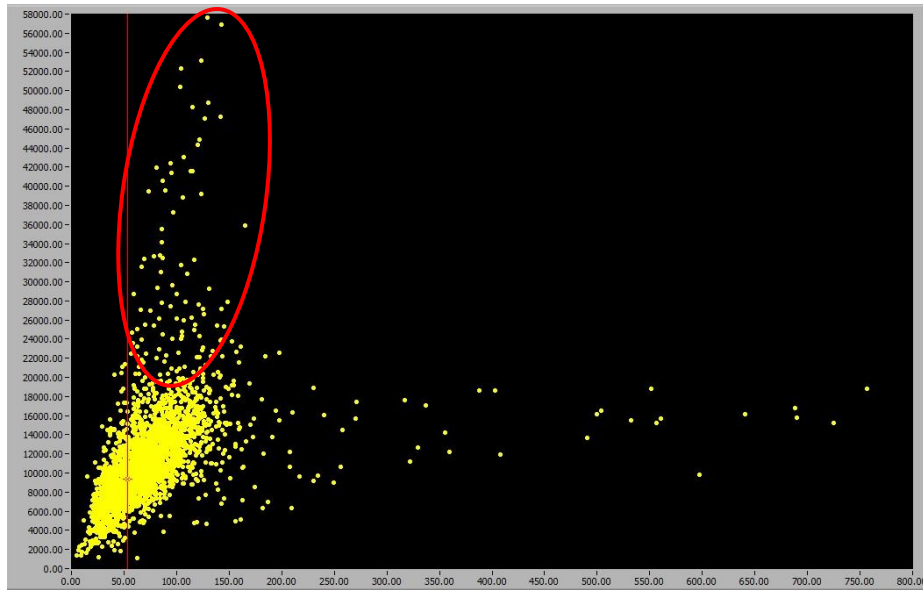
Figure 43 Aff16 sample, correlation plot between FeKa counts (y axis) and TiKa counts (x axis) of 2D measurement
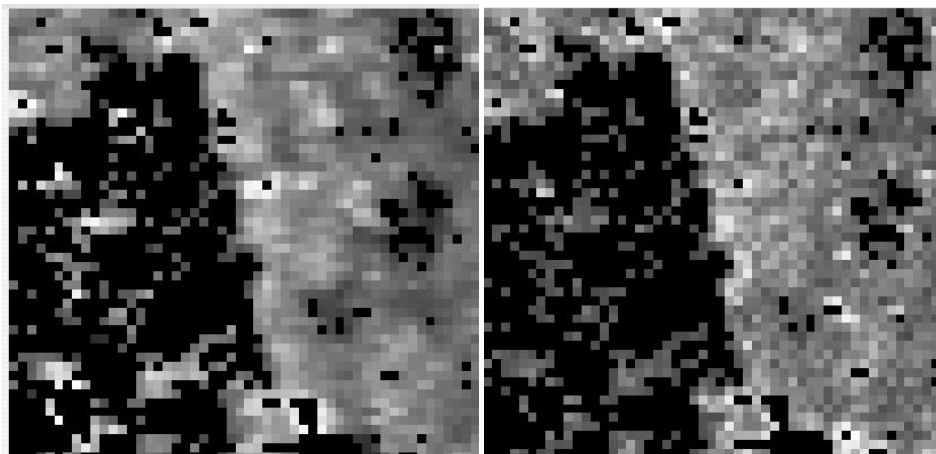
Figure 44 Aff16 sample, photos of FeKa (left) and TiKa (right) of chosen area

The photos (*Figure 44*) reveal another correlation of Fe with the element Ti also in the green earth pigment, but the statistic of Ti is also very low.

In the same area a 3D measurement was also conducted. The major elements, Fe (green), Ca (red) and K (blue) were visualized through the use of ImageJ 1.52a and Icy 1.9.9.1 softwares in a three dimension model.
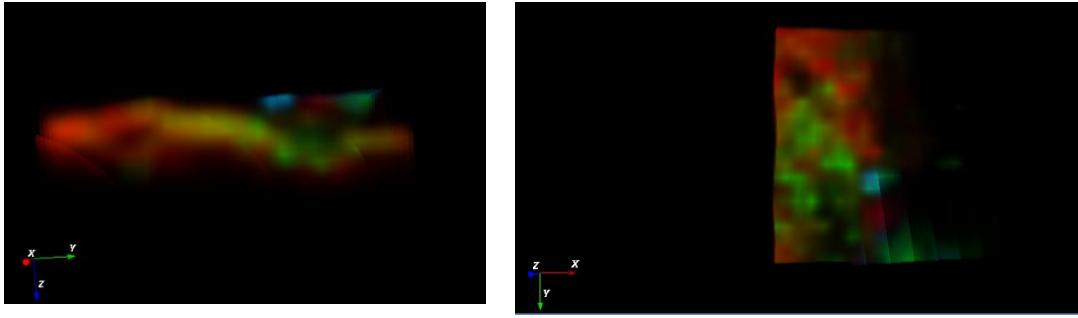
Figure 45 Side and front photos of 3D model of Aff16 sample, Ca, Fe and K are presented with red, green and blue respectively

From the reconstruction of the 3D model (*Figure 45*) of the color layers of the sample it is clear that Ca, hence the preparation, appears in the bottom and Fe and K appear successively above it as the layer of ochre and green earth.

AFF4 (BN10)

For the 2D measurement the chosen area was between the light green and the white area (*Figure 46*).
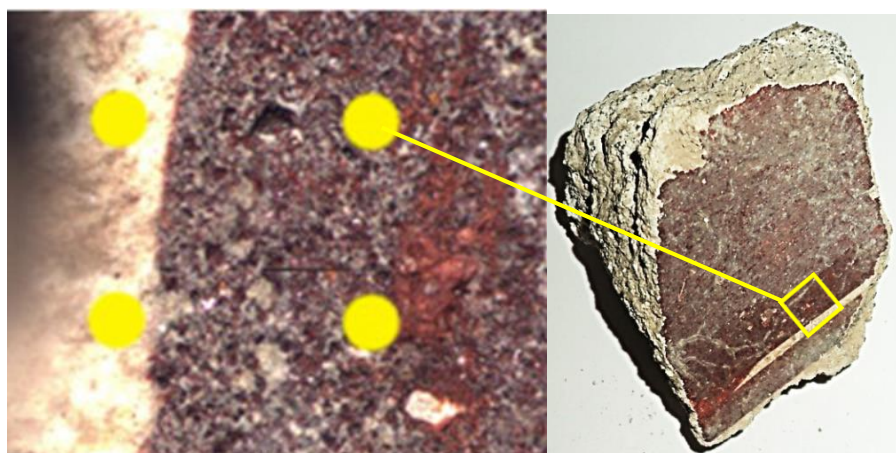


Figure 46 Aff4 microscopic photo 1 x 1 mm of chosen area
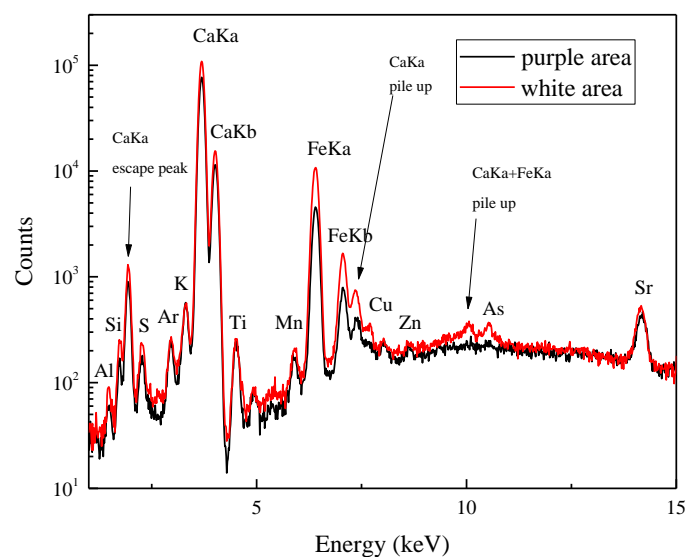
Figure 47 Aff4 sample, purple ochre pigment (2nd layer), white lime based pigment (top layer), ROI spectra of the 2D measurement

In Aff4 sample spectrum (*Figure 47*) it is visible that the white area presents more Fe than the purple area. In the purple area the major elements are Ca which is assigned to the lime preparation and Fe which is assigned to reddish purple hue. In the white area of the sample the major elements is Ca and Fe but the counts of Fe are fewer than the ones visible in the purple area. Other elements like Al, Si, S, K, Ti, Cr, Mn. Cu, Zn and Sr are also present as minor elements in both areas.

Some correlations between elements of the sample were observed through the creation of their scatter plots from the 2D measurements and their analysis with XRF Imaging rev software.
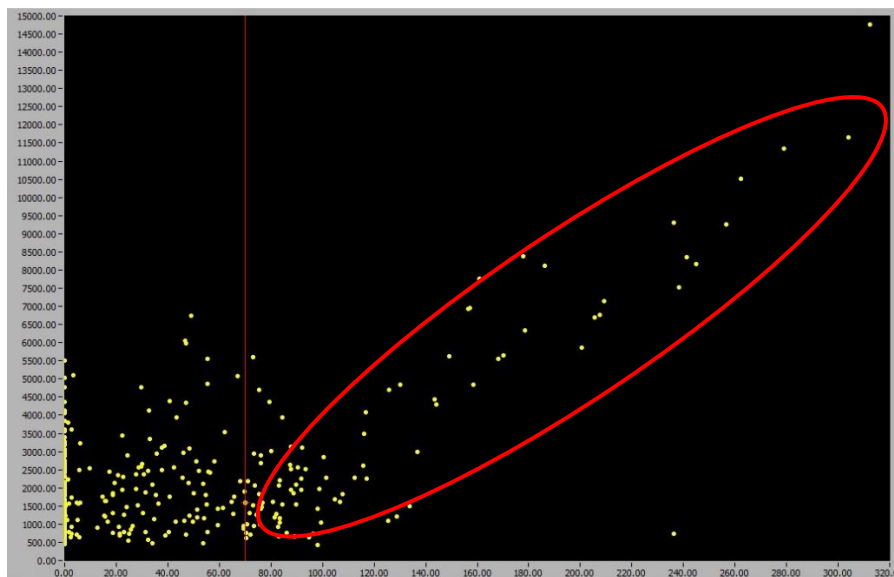
Figure 48 Aff4 sample, correlation plot between FeKa counts (y axis) and AsK counts (x axis) of 2D measurement

The two elements show a correlation (*Figure 48*) but the As has low statistics in contrast to Fe.
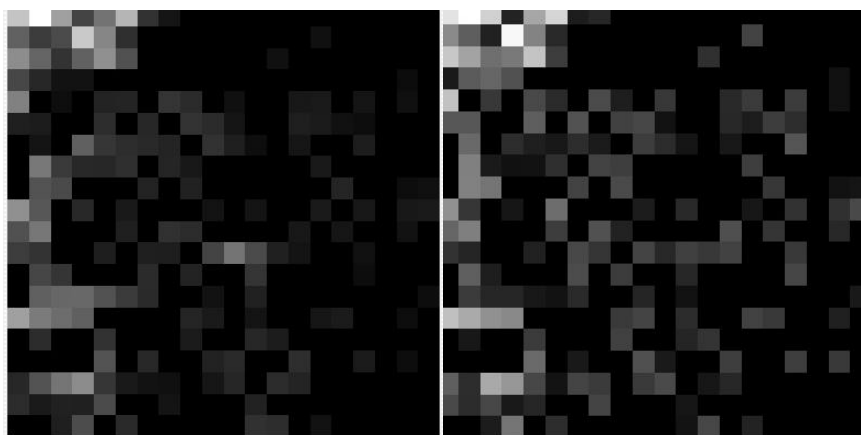
Figure 49 Aff4 sample, photos of FeKa (left) and AsK (right) from chosen area

From the photos extracted from the chosen area (*Figure 49*), a correlation appears between the elements in the white area but not a strong one.

Another correlation appears to the scatter plot between Si and K counts (*Figure 50*).
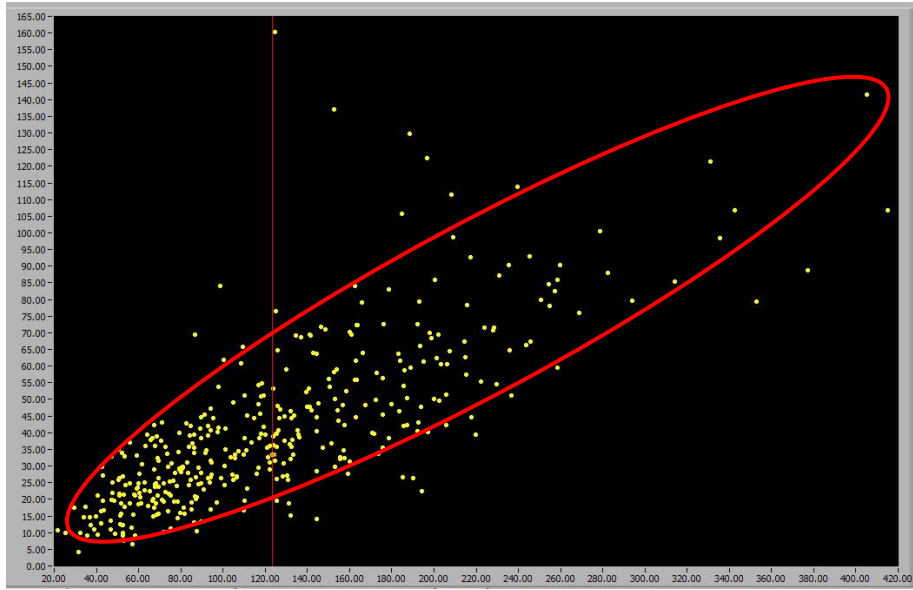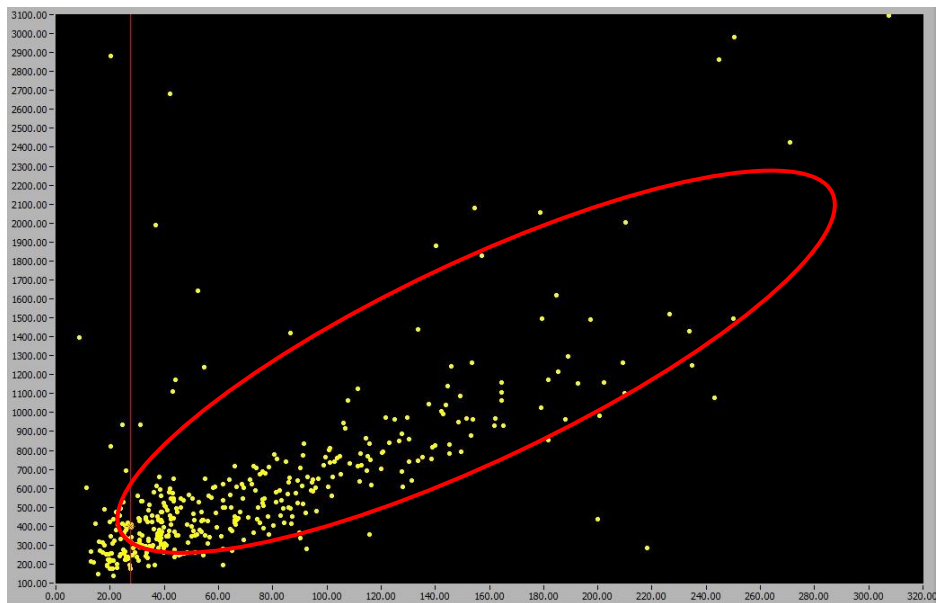
*Figure 50 Aff4 sample, correlation plot of SiK counts (y axis) and KKa counts (x axis) of the 2D measurement*
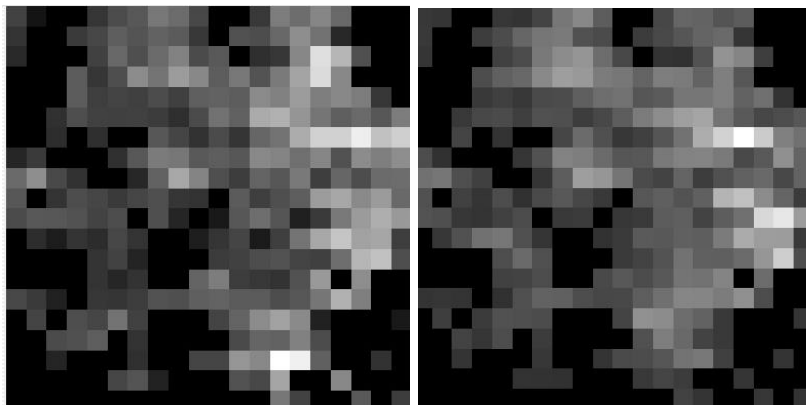
Figure 51 Aff4 sample, photos of SiK (left) and KKa (right) from chosen area

Although the statistics of neither of the elements is big, they appear in the same area of the sample (*Figure 51*).

AFF2 (BN9)

For the 2D measurement the chosen area was between the bright red and the purple area (*Figure 52*).
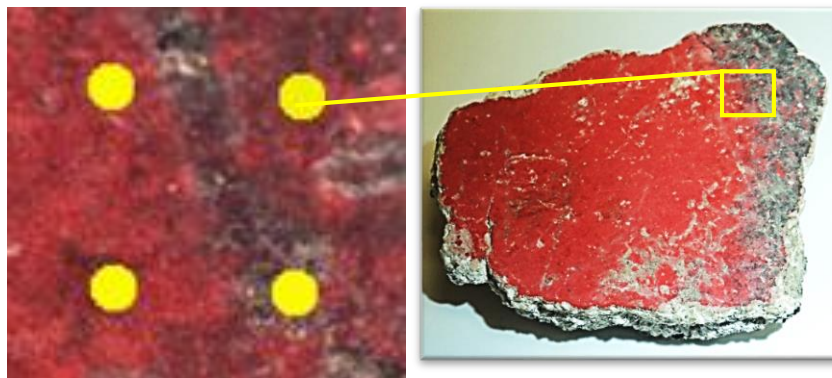
Figure 52 Aff2 microscopic photo 0.8 x 0.8 mm of chosen area
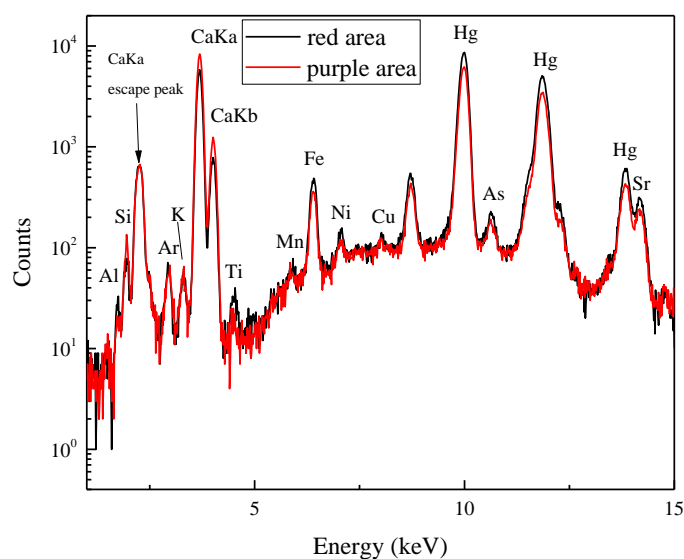
Figure 53 Aff2 sample, purple ochre pigment (top layer), cinnabar pigment (2nd layer), ROI spectra of the 2D measurement

In Aff2 sample (*Figure 53*) there are very small differences between the red and the purple areas. The red area appears more abundance of Hg in comparison with the purple area. The red area presents Ca and Hg as major elements which show the presence of the lime preparation and cinnabar as a paint layer, respectively. In the purple area the major elements also are Ca and Hg. In both spectra it is visible the high counts of Fe which is

due to the mixing of cinnabar with red ochre (hematite). The rest of the elements (Al, Si, S, Ar, K, Ti, Mn, Ni, Cu, As and Sr) appear as minor elements in both spectra. The preparation layer in all samples is calcium based, probably lime as it was a common material in wall – paintings in roman times.

From the 2D measurement scatter plots were created through the use of XRF Imaging Rev software that show the correlation of some elements between them and with the color layers of the sample.

Figure 54 Aff2 sample, correlation plot of FeKa counts (y axis) and KKa counts (x axis) of the 2D measurement
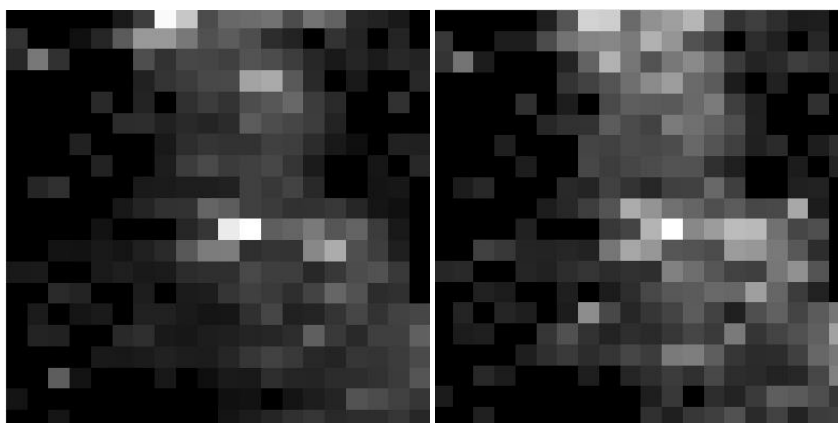
Figure 55 Aff2 sample, photos of FeKa (left) and KKa (right) of the chosen area

In the correlation plot the counts of Fe and K were plotted (*Figure 54*). The photos that extracted show the correlation of the two elements with the color layers of the sample

(*Figure 55*). It is visible that Fe and K appear in the same area where the purple line exists in the sample.

Another correlation appears between Fe and Ti in the sample (*Figure 56*).
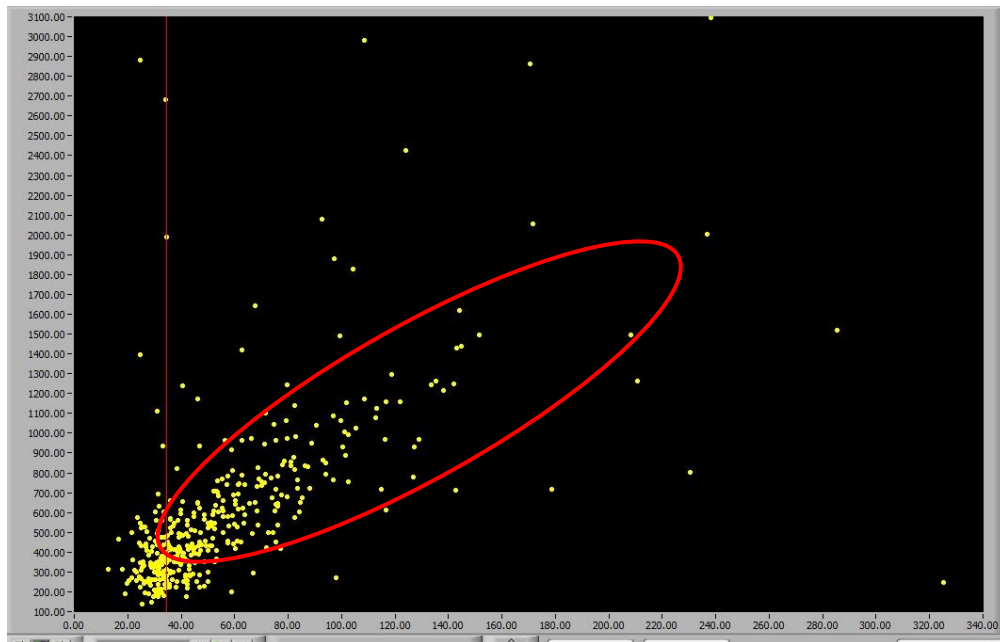
Figure 56 Aff2 sample, correlation plot between FeKa counts (y axis) and TiKa counts (x axis) from 2D measurement
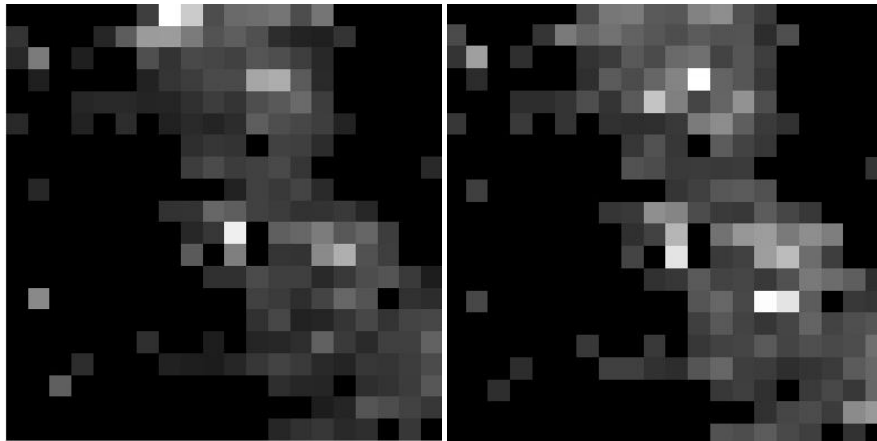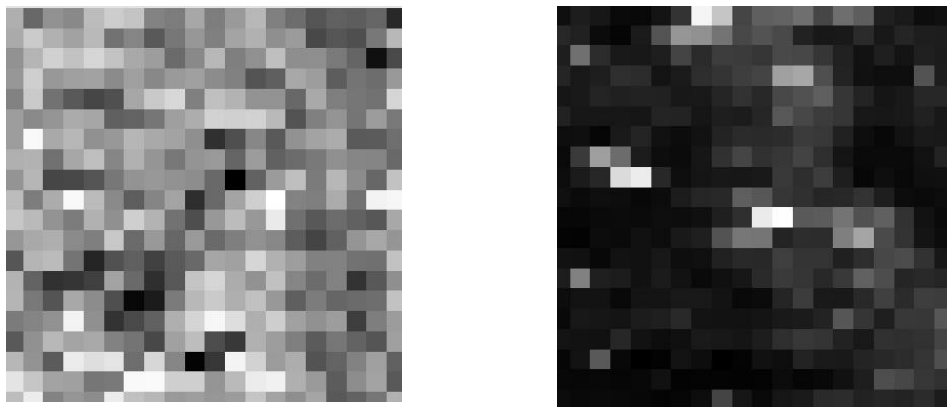

Figure 57 Aff2 sample, photos of FeKa (left) and TiKa (right) of the chosen area

In the photos extracted from the chosen area (*Figure 57*) of the scatter plot it is clear that Fe and Ti appear in the area of the purple line in the sample.

However, in both correlation plots presented above the statistics of the elements are not so good, but enough to show a correlation.

Two more correlations were made between Hg and Fe and Hg and Zn in the sample (*Figure 58*, *Figure 60*).
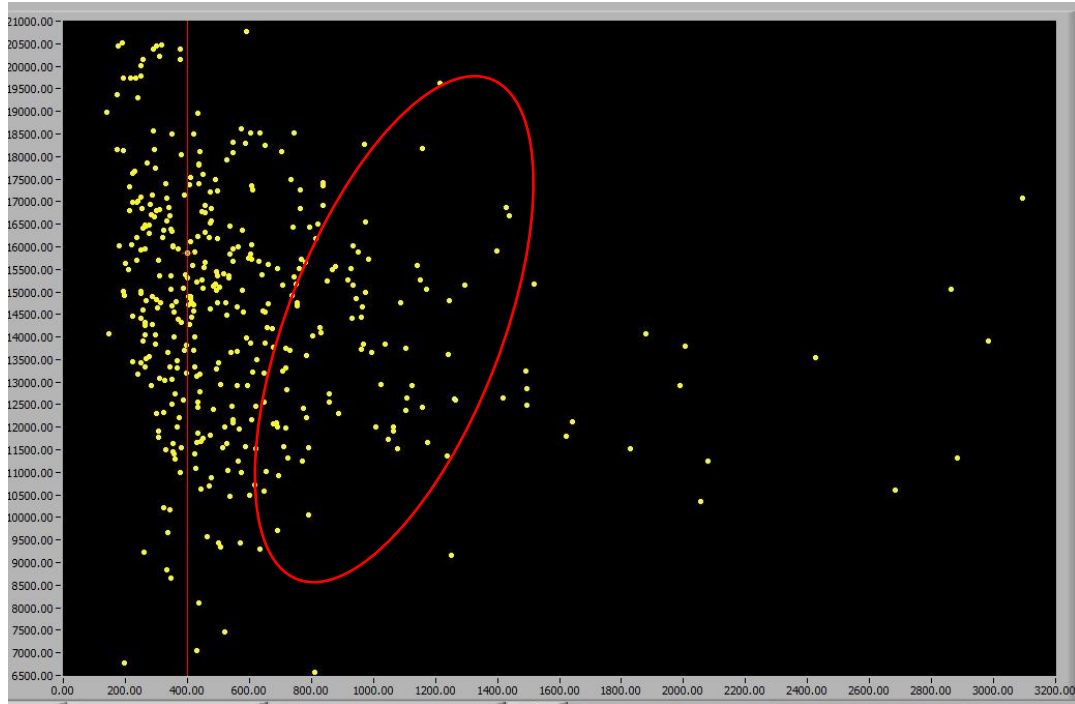
Figure 58 Aff2 sample, correlation plot between HgL3 counts (y axis) and FeKa counts (x axis) from 2D measurement

Figure 59 Aff2 sample, photos of HgL3 (left) and FeKa (right) of the chosen area

In the photos extracted from the chosen area (*Figure 59*) of the scatter plot it is clear that Hg and Fe do not appear a big correlation although the statistics of the elements is large enough. However, in both correlation plots presented above the statistics of the elements are not so good, but enough to show a correlation.
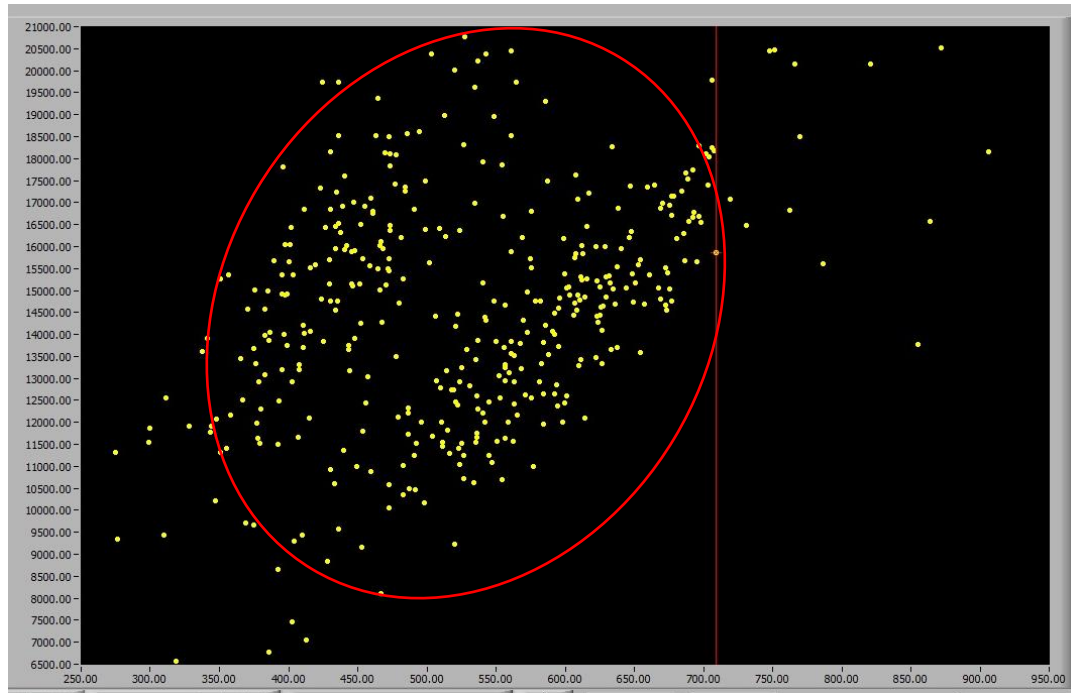
Figure 60 Aff2 sample, correlation plot between HgL3 counts (y axis) and ZnKa counts (x axis) from 2D measurement
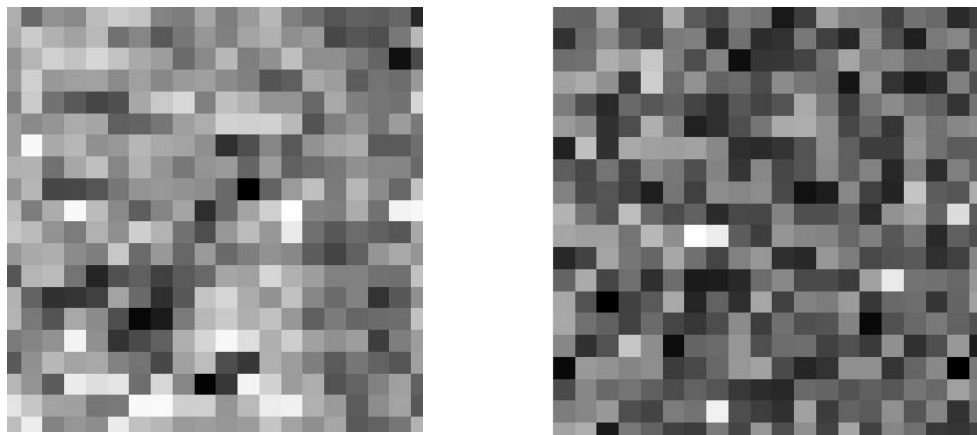
Figure 61 Aff2 sample, photos of HgL3 (left) and ZnKa (right) of the chosen area

From the photos extracted from the chosen area of the plot (*Figure 61*) a correlation appears between Hg and Zn. Both of the elements appear in the whole area of the 2D measurement and with the same intensity.

In the same area of the 2D measurement, a 3D measurement was also conducted. The major elements, Fe (green), Ca (red) and Hg (blue) were visualized through the use of ImageJ 1.52a and Icy 1.9.9.1 softwares in a three dimension model.
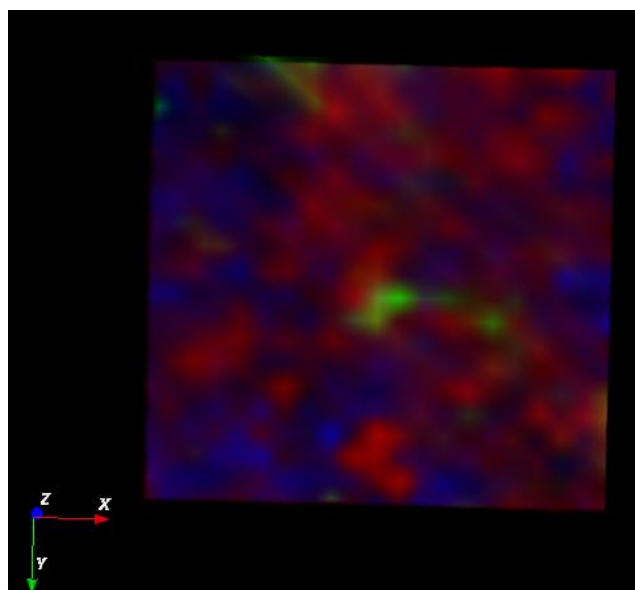
Figure 62 3D model photo (on top) of Aff2 sample, Ca, Fe and Hg are represented with red, green and blue respectively
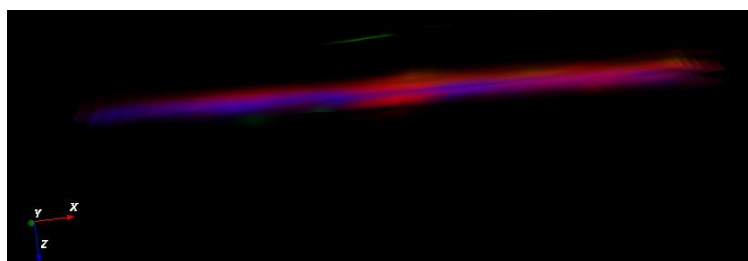
Figure 63 3D model side photo of Aff2 sample, Ca, Fe and Hg are represented with red, green and blue respectively

In the 3D model (*Figure 62*) that was created it is visible that Ca and Hg are in abundance. With a closer and more meticulous look it is clear that the Ca in the photo creates a trend that resembles to the purple line in the sample, while Hg seems to be all around it. The Fe in the photo appears along that trend but not so intense to create a more uniform layer. In the side photo (*Figure 63*) of the 3D model it is clear that the layer of ochre is on the top while the layer of cinnabar (HgS) is lower.

Summary of Domus Benedictine analytical results

In the samples presented above three main pigments were identified, ochre (hematite and/or goethite), green earth (celadonite and/or glauconite) and cinnabar. Different

treatments of the mentioned pigments also appear, e.g. in the sample Aff4 heated hematite creates that purple hue that is visible in the sample as well as in the sample Aff2 where cinnabar is mixed with ochre for the creation of a more intense color result. In sample Aff16 a strong correlation is observed between Fe and K, Fe and Si and Fe and Ti in the area where the green earth pigment is. In the same sample the 3D model that was constructed clearly shows the stratigraphy of the pigments, with calcium based preparation followed by ochre pigment and green earth pigment on top.

In sample Aff2 correlations appear between Fe and Ti and Fe and K where the purple line is. The 3D model that was constructed in the sample Aff2 shows clearly where Hg, Ca and Fe are in the sample.

Table 5 presents the suggested pigments of each sample according to their spectra.

Table 5 Samples' suggested pigments

Sample	Site	Color of the paint layer/Description	Major element	Suggested pigment	Minor elements	Trace elements	Preparation layer element	Preparation layer
A8	Villa del Casale	yellow/orange	Fe	ochre	K, Mn, Cu, Zn, As, Sr	Al, Cr, Ti, Si, S	Ca	Lime
#48	Villa del Casale	yellow/orange	Fe	ochre	Mn, Cu, As, Sr	Al, Cr, Ti, Zn	Ca	Lime
#48	Villa del Casale	green	Fe, K, Si	Green Earth (celadonite/ glauconite)	Mn, Cu, As, Sr	Al, Cr, Ti, Zn	Ca	Lime
#57	Villa del Casale	red	Fe	ochre	K, Cu, As, Sr	Al, Cr, Ti, Zn, Si, S, Mn	Ca	Lime
Sample 1	Villa del Casale	light yellow/orange	Fe	ochre	Si, K, Zn	Al, S, Ti, Mn, Pb, Sr	Ca	Lime
Sample 1	Villa del Casale	light blue/green	Cu	Malachite or Verdigris or Azurite	Si, K	Al, S, Ti, Mn, Zn, Pb, Sr	Ca	Lime
Aff16	Benedectine Monastery	red	Fe	ochre	Si, Mn, Cu, Zn, As, Sr	Al, S, Ti, Cr	Ca	Lime
Aff16	Benedectine Monastery	green	Fe, K, Si	Green Earth (celadonite/ glauconite)	Mn, Cu, Zn, As, Sr	Al, S, Ti, Cr	Ca	Lime
Aff4	Benedectine Monastery	reddish purple	Fe	ochre (heated hematite)	K, Ti, Cu, Zn, As, Sr	Si, S, Al, Cr, Mn	Ca	Lime
Aff2	Benedectine Monastery	purple	Fe	ochre	Al, Si, K, Ti, Mn, Ni, Cu, As, Sr	Al,K, Ti, Mn, Ni	Ca	Lime

| Aff2 | Benedectine Monastery | dark red | Hg, S | Cinnabar | Al, Si, K, Ti, Mn, Ni, Cu, As, Sr | Al,K, Ti, Mn, Ni | Ca | Lime |

6.3 In-depth (1D) measurements results

In every in-depth measurement (1D) taken in each sample, the thickness of the paint layer was measured. This was succeeded by the following function:

$$Thickness(i) = \sqrt{FWHM(s)^2 - FWHM(p)^2}$$

Where FWHM (s) =full width at the half maximum of the characteristic x-ray line of an element from the sample

FWHM (p) = full width at the half maximum of the characteristic x-ray line of the pure element (micro-matter target)

Table 6 presents the thickness of each paint layer as well as the maximum counts of Ca and the major element of every measurement and the depth difference of the maximum intensity of each layer.

Table 6 Thicknesses of paint layers

Fragment	Element	Spot	Max (counts)	Difference of maximum counts: major element vs Ca (µm)	Thickness (µm)
#48	FeKa	Yellow on blue	4327	-5	18
	CaKa	Yellow on blue	4515		-
	KKa	Yellow on blue	254		13
#48	FeKa	Yellow on blue	6848	-5	22
	CaKa	Yellow on blue	5864		-
	KKa	Yellow on blue	345		16
#57	FeKa	Red	4612	-0.5	21
	CaKa	Red	5428		-
#57	FeKa	Red	3804	5	16
	CaKa	Red	6958		-
#57	FeKa	Red	10284	0	20
	CaKa	Red	4703		-
Aff4	FeKa	White	449	4	14

	CaKa	White	14433		-
Aff4	FeKa	Purple	31902	5	17
	CaKa	Purple	6645		-
Aff4	FeKa	Purple	34768	-1.5	21
	CaKa	Purple	8255		-
Aff4	FeKa	Purple	30559	5	22
	CaKa	Purple	6933		-
Sample 1	FeKa	Yellow on blue	1468	0	33
	CuKa	Yellow on blue	-	-	Negative
	CaKa	Yellow on blue	4908		-
Aff16	FeKa	Green	6996	1	29
	KKa	Green	485	-	23
	CaKa	Green	2445		-
Aff16	FeKa	Red	4815	20	69
	CaKa	Red	5882	-	-
Aff2	CaKa	Red	2049		-
	HgL3	Red	6910	-10	15
	FeKa	Red	146		17
Aff2	CaKa	Red	4284		-
	HgL3	Red	5087	-10	22
	FeKa	Red	95		19
Aff2	CaKa	Purple	4393		-
	HgL3	Purple	5448	-5	21
	FeKa	Purple	1107		22
Aff2	CaKa	Purple	5205		-
	HgL3	Purple	5501	-20	29
	FeKa	Purple	1262		58
A8	FeKa	Yellow	7278	-1	Negative
	CaKa	Yellow	7781		-
A8	FeKa	Yellow	10773	1	Negative
	CaKa	Yellow	8254		-
A8	FeKa	Yellow	5389	2	Negative
	CaKa	Yellow	9123		-

The thickness of each paint layer of each sample is visible in the table. In some samples Ca maximum counts appear closer to the surface than the ones coming from the major element of each paint layer. This phenomenon is due to the fresco technique and the lime solution used as binder of the pigments that were used for the creation of the wall paintings.

Samples A8 and Sample 1 present negative numbers for the thickness of their paint layers for Fe and Cu respectively. This is a statistical error which shows that the real thickness of the paint layers is much smaller than the FWHM of their scatter plots.

The following plots present the in-depth (1D) elemental profiles of the major elements of each sample. When a layer is thin (20-30 μm) appears as a Gaussian function. When it is thick enough (>50 μm) creates a Gaussian function but also a decay function as going deeper into the sample.
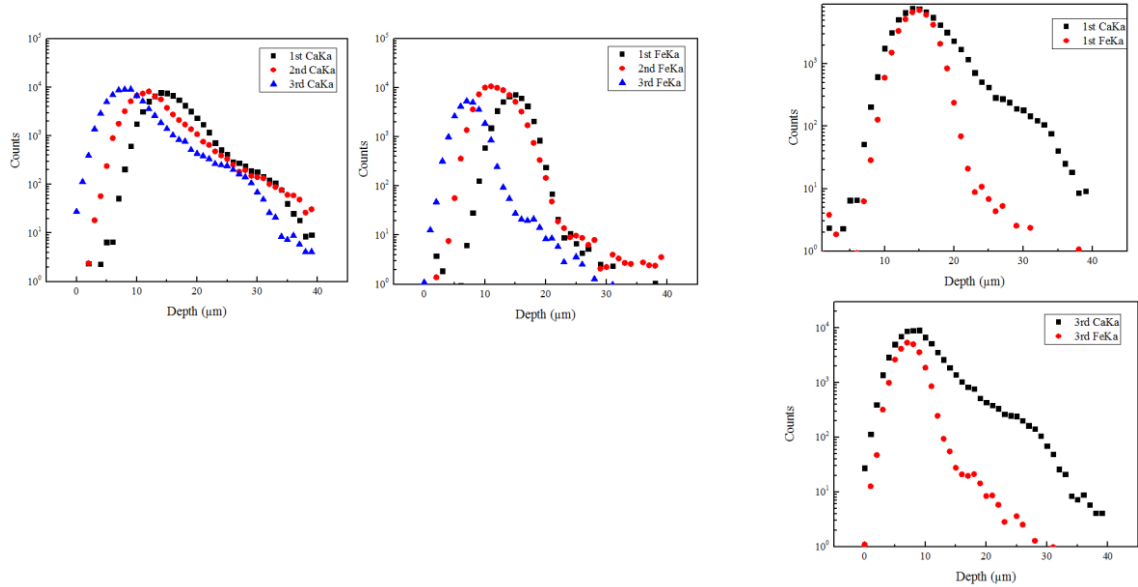
Figure 64 A8 sample, yellow ochre pigment, depth profiles of Ca and Fe from all the 1D measurements of the specimen (left)

A8 sample, depth profiles of CaKa and FeKa of the same 1D measurements (right)
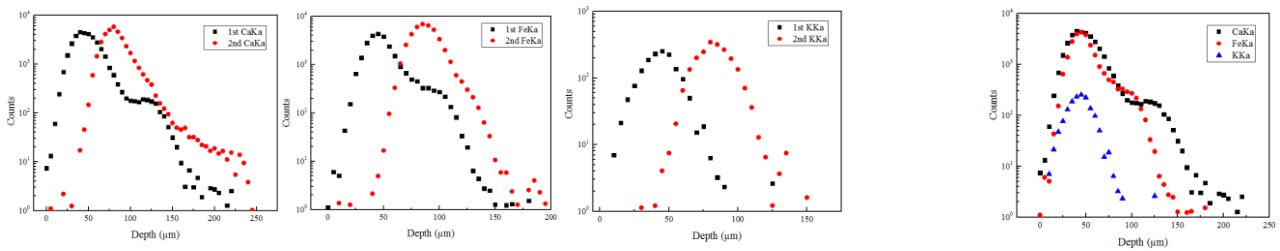
Figure 65 #48 sample, green earth pigment (top layer), yellow ochre pigment (2nd layer), depth profiles of Ca, Fe and K from all the 1D measurements of the specimen (left)

#48 sample, depth profiles of Ca, Fe and K from the same measurement (right)
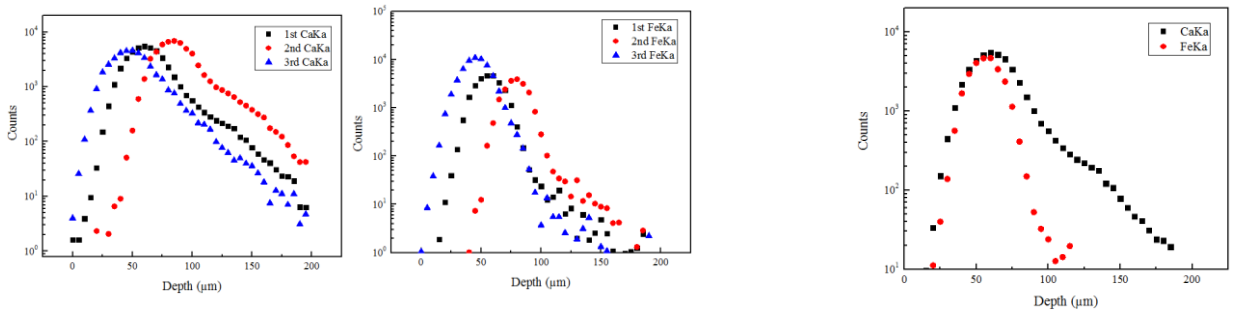
Figure 66 #57 sample, red ochre pigment, depth profiles of Ca (right) and Fe (left) for all three (3) 1D measurements (left)

#57 sample, depth profiles of Fe and Ca from the same 1D measurement (right)
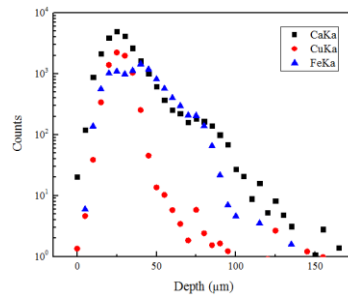
Figure 67 Sample 1, azurite or malachite pigment (top layer), yellow ochre pigment (2nd layer) depth profiles of CaKa, FeKa and CuKa of the 1D measurement
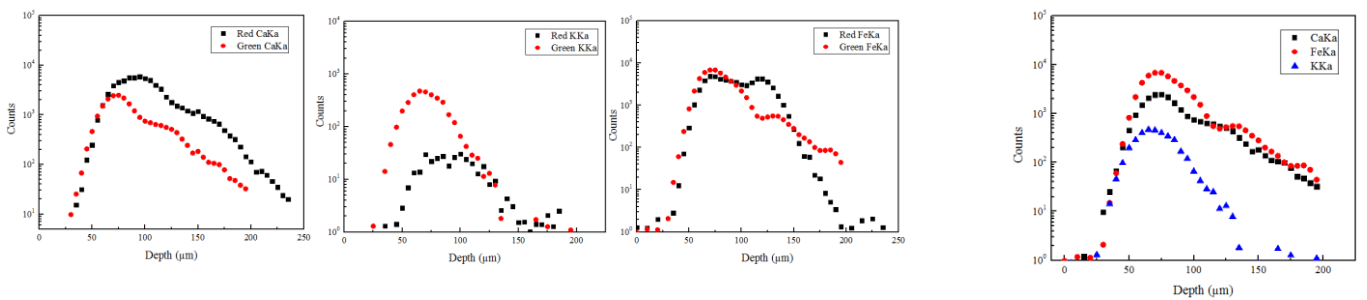
Figure 68 Aff16 sample, green earth pigment (top layer), red ochre (2nd layer) depth profiles of CaKa , FeKa and KKa from the two (2) 1D measurements (left)

Aff16 sample, depth profiles of CaKa, FeKa and KKa from the green area of 1D measurement (right)
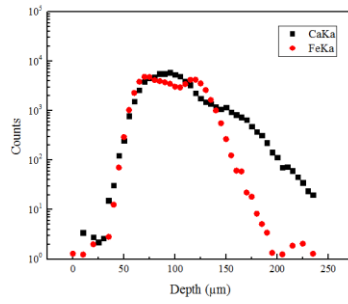
Figure 69 Aff16 sample, green earth pigment (top layer), red ochre (2nd layer) depth profiles of CaKa and FeKa from the red area of 1D measurement
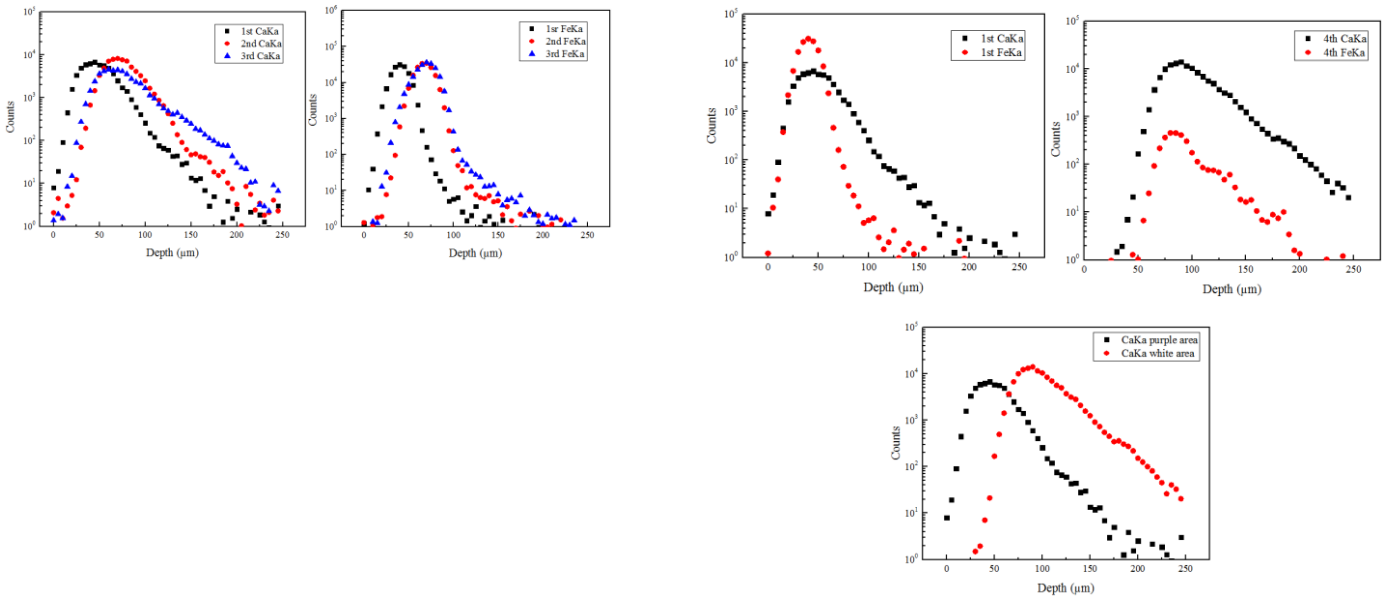
Figure 70 Aff4 sample, purple ochre (top layer) depth profiles of CaKa and FeKa of the 1D measurements in the purple areas (left)

Aff4 sample, depth profiles of Ca and Fe from one of the purple area and the white area (right) and depth profile of Ca from the white and the purple area (right bottom)
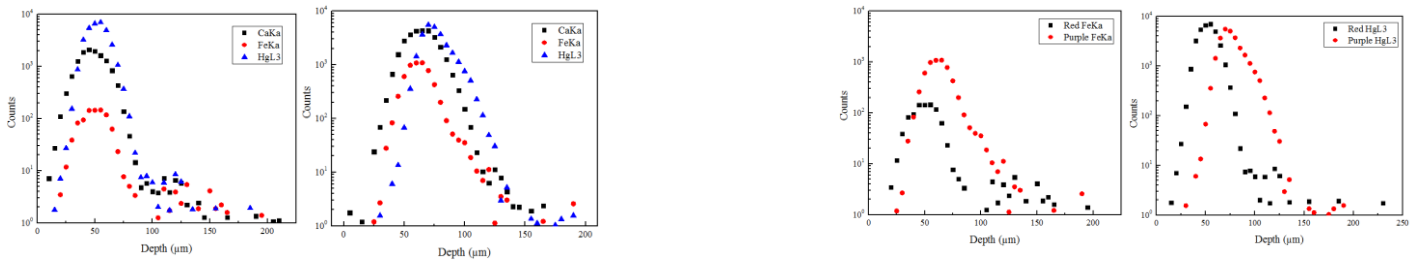
Figure 71 Aff2 sample, depth profiles of CaKa, FeKa and HgL3 from 1D measurements, in the red cinnabar area and in the purple ochre area (left)

Aff2 sample, depth profiles of FeKa and HgL3 from two 1D measurements (red area and purple area) (right)

A similarity is visible in the depths where the maximum counts of the elements from the same measurements are. The difference in the depths of the maximum counts of the elements of each sample (between same elements) that is visible in most of the samples is a result of the anomaly of the samples surface. As mentioned previously the pigments used to be mixed within a solution of lime plaster for their application on the wall – painting, so this is why top and lower paint layers maximum counts appear together in the same depth. Another explanation to the early depth appearance of some elements is assigned to the use of fresco technique, so a mixing of the layers is expected.

It is observed that the depth profiles of an element from the same sample but different measurements, appear a uniformed distribution towards depth as it is obvious in A8 sample (*Figure 64*).

In all samples calcium appears in the same or almost the same depth as the characteristic elements of the pigments.

Also, Ca depth profiles appear more extended. The width of Ca depth profiles could be narrower than it appears. This is explained as a statistical error and that is why Ca appears closer to the surface than the centroid of the major element of each paint layer as appeared in **Table 6**.

In all samples the depth profiles of the dominant elements clearly show the different layers that are formed.

A8 sample has one yellow ochre paint layer. The depth profiles of Ca from the A8 sample show a similar trend. It appears that Ca is detected from two different depths, hence two layers, the preparation layer and the color layer of the ochre. The depth profiles of Fe create Gaussian profile which is assigned in the layer of ochre (*Figure 64*). In the scatter plot of A8 sample the depth profiles of Ca and Fe are combined, where it is visible that the maximum counts of both of the elements appear almost in the same depth.

Sample #48 has two layers, the top paint layer of green earth contains in its composition K and Fe while the second layer of ochre contains Fe. The thickness of green earth is around 12-16 μm as it is obvious from K thickness in **Table 6**. From the depth profile of Fe the thickness of the paint layer that contains Fe seems to be 18-22 μm but green earth and yellow ochre have both Fe in their composition.

The depth profiles (*Figure 65*) of CaKa from the two measurements appear the same tendency. Calcium creates two peaks which means that is detected in two different depths, hence two layers. The same behavior is visible in the Fe scatter plots, one peak coming from the layer of green earth pigment while the other peak comes from the underneath layer of ochre pigment. It is interesting to observe that K, Fe maximum counts appear in the same depth so it is normal to see them together but Ca maximum counts that comes from the below layers of ochre and preparation (lime) indicates the rising of the preparation closer to the surface or the dissolving of pigments within saturated aqueous solution of lime for their application in the damp lime plaster (Balandier *et al.*, 2017).

#57 sample has one red ochre paint layer which thickness seems to be around 15-20 μm as it is obvious from Fe thickness in **Table 6**. The depth profiles (*Figure 66*) of Ca appear all the same tendency with the creation of a wide peak that spreads deeper into the sample. On the first and second depth profiles of Ca a clearer image of a second smaller peak is created, in contrast with the third measurement, which shows the existence of two layers of Ca in the sample, one coming from the layer of the ochre and the other from the preparation layer. The depth profiles of Fe are represented with Gaussian profile but a bit extended towards depth which are assigned in the layer of ochre.

In Sample 1 sample the depth profiles Ca, Fe and Cu are presented in a scatter plot (*Figure 67*) and are assigned to a malachite or azurite pigment as top paint layer. Underneath a yellow ochre pigment exists. The Fe depth profile show a thickness of the paint layer containing Fe around 16-21 μm. Fe presents a fluctuation with the first peak coming from the malachite or azurite layer and the second peak coming from the lower ochre pigment. Ca creates two peaks with the second peak coming from the preparation layer. Deeper in the sample Fe seems to exist in another layer, probably an impurity in the preparation layer.

In Aff16 sample the depth profiles (*Figure 68, Figure 69*) of Ca, Fe and K from the green and the red area are presented in scatter plots. The thickness of green earth is around 23-29 μm as it is visible from **Table 6**. The thickness of red ochre pigment paint layer is 68.99 μm. The elements of Fe, Ca and K are assigned to the green earth pigment which is the top layer while Fe and Ca are assigned to the layer of red ochre which is the paint layer underneath. In the scatter plot of Fe two peaks are created which shows that both of the paint layers containing it. The first peak of Fe from the red area coincides with the maximum counts peak of the green area. The fact that two peaks are visible in the

Fe scatter plot of the red area shows that although the red area is the underneath layer, it probably has a thin layer of green earth pigment on the top that creates the second peak. In the Ca scatter plot the two peaks that are created come from the two different paint layers and not from the lime preparation layer.

K is assigned to the green earth pigment layer but the red ochre pigment also contains it as a minor element. This can be explained from the K scatter plot that creates a Gaussian profile but seems extended towards depth. In the scatter plot of K it is clear that the potassium coming from the green area is much higher in counts than the one coming from the red area.

In Aff4 sample the depth profiles (*Figure 70*) of Ca and Fe extracted from the measured purple and white areas are presented. Ca and Fe are assigned to the purple ochre area. The thickness of purple ochre pigment paint layer is around 16-21 μm as it is visible in **Table *6***. Ca is also assigned to the white area. The depth profiles of calcium appear all a peak and stretch deeper. All of them indicate a second layer of Ca which is better visible in the second and third measurement with the creation of smaller peaks. The depth profiles of Fe seem similar each of them with a distinct peak that represent the layer of ochre. The combined scatter plots of Ca and Fe depth profiles from one of the purple area and the white area are presented. In the scatter plot of the purple area the calcium and iron appear together, however their peaks have a slight depth difference which indicates that the iron comes first as the top layer. The larger number of counts of Fe in contrast with Ca is another indication of the existence of the ochre layer. In the scatter plot extracted from the white area, Ca appears in abundance on the contrary to Fe. In the scatter plot of Ca from one of the purple areas and the white area, the white area seems to have more counts of Ca than the purple area but it creates a broader depth profile with a decay function as going deeper which means the presence of Ca from the layer of white on the top and the layer of ochre underneath.

In Aff2 sample the scatter plots (*Figure 71*) present the depth profiles of the three major elements (Ca, Fe, Hg) in the sample, in the red area and in the purple. Fe and Hg are assigned to the red area, hence the area of cinnabar pigment and Fe also is assigned to the purple area, hence the area of ochre pigment. Fe comes from ochre, but as mentioned earlier it was used in the creation of the wall – painting as an admixture to the pigment of cinnabar. The paint layer of cinnabar has thickness around 15-23 μm while purple ochre area has a thickness 22-58 μm as it is visible in **Table *6***. The centroid of the Fe depth profile appears earlier, while the centroid of the Ca depth profile comes after and

the one of Hg last. That shows the use of more ochre in the sample or even an extra layer of ochre on top of the one with cinnabar that also changes the color from red to purple. The depth profiles of Ca, Fe and Hg from the 1D measurements were compared between the red and the purple area. In the scatter plot of Fe from the purple area it is visible that the depth profile of Fe creates two peaks which show the existence of Fe in the purple ochre area and the red cinnabar area. The same behavior is visible in the scatter plot of Hg from the purple area. In the calcium scatter plot, the Ca seems more in abundance in the purple area. The same thing is observed also in the iron depth profiles, where Fe appears more counts in the purple area.

7   Discussion

For this study seven (7) roman wall – painting fragments were analyzed, along with eighteen (18) micro matter targets.

The measuring of the micro matter targets helped to the establishment of the correct working of the XRF system.

The 2D application of micro XRF allowed us to observe not only the composition of each sample and the intense of their elements but also to picture it and watch where each element exists in each sample's surface. The pigments that were identified from all samples are green earth, ochre, malachite/azurite/verdigris and cinnabar.

Through 2D measurements some qualitative correlations revealed between the analyzed objects containing ochre in their composition. In three roman wall – painting fragments (Samples: #48, Aff16, Aff2), Fe forms a strong correlation with K. In two more roman wall – painting fragments (Samples: Aff16, Aff4), Fe forms correlation with As. In samples #48 and Aff4 another correlation appears between Si and K. Last correlation appears between Fe and Ti in samples Aff16 and Aff2. So it can be assumed that these elements are color dependent to the pigment ochre.

It was observed that in all roman wall – painting fragments a calcium based preparation was used for their construction which is assigned to lime according to bibliographical sources already mentioned.

The micro confocal XRF with the 1D and 3D applications provided useful information and a gaze into the structure and stratigraphy of the samples. It became able to measure the amount of layers in each sample, as well as to see how each layer forms and penetrates another. The in-depth (1D) measurements helped to measure the thickness of each paint layer. However through this application it was observed that in some of the roman wall – painting fragments Ca appears in the same depth together with the paint layers. So it is unclear if the Romans used a saturated aqueous solution of lime to apply the pigments in the damp plaster or Ca was risen through the different layers by the passing of time.

Analysis of wall – painting fragments with XRF applications has proven to be useful to the understanding of the ways the wall – paintings were structured in ancient times as well as to come across to qualitative results about the materials used.

8   Future work/ Perspectives

Although many sources inform about the roman techniques used for the creation of wall – paintings, this essay should be a start to explore better their structure through applications.

The analysis of a wide range of roman wall – paintings could give a general view of the techniques and the pigments used. Through the construction of wall – painting mock-up samples the characteristic properties of each technique can be explored and established for future analysis.

Correlations between elements could give a starting point for the exploration of trace elements on pigments or the pigments' behavior when combining with other materials.

This essay can be expanded with introducing complementary methods of analysis for the identification and exploration of wall – painting stratigraphy and pigments.

9 References

Aliatis, I. *et al.* (2010) 'Pigments used in Roman wall paintings in the Vesuvian area', *Journal of Raman Spectroscopy*, 41(11), pp. 1537–1542. doi: 10.1002/jrs.2701.

Bakiler, M. *et al.* (2016) 'Material characterization of the Late Roman wall painting samples from Sinop Balatlar Church Complex in the black sea region of Turkey', *Microchemical Journal*, 126, pp. 263–273. doi: 10.1016/j.microc.2015.11.050.

Balandier, C. *et al.* (2017) 'Chemical analyses of Roman wall paintings recently found in Paphos, Cyprus: The complementarity of archaeological and chemical studies', *Journal of Archaeological Science: Reports*. Elsevier, 14(January), pp. 332–339. doi: 10.1016/j.jasrep.2017.06.016.

Bardelli, F. *et al.* (2011) 'Combined non-destructive XRF and SR-XAS study of archaeological artefacts', *Analytical and Bioanalytical Chemistry*, 399(9), pp. 3147–3153. doi: 10.1007/s00216-011-4718-8.

Caliri, C., Francesco, S. and Romano, P. (2017) 'A MOBILE XRF SCANNER FOR A REAL-TIME ELEMENTAL IMAGING OF PAINTED ARTWORKS', (January).

Debastiani, R. *et al.* (2016) 'Identification of green pigments from fragments of Roman mural paintings of three Roman sites from north of Germania Superior', *Applied Physics A: Materials Science and Processing*. Springer Berlin Heidelberg, 122(10). doi: 10.1007/s00339-016-0400-5.

Duran, A. *et al.* (2010) 'Determination of pigments and binders in Pompeian Wall paintings using synchrotron radiation - high-resolution X-Ray powder diffraction and conventional spectroscopy - chromatography', *Archaeometry*, 52(2), pp. 286–307. doi: 10.1111/j.1475-4754.2009.00478.x.

Elias, M. *et al.* (2006) 'The colour of ochres explained by their composition', *Materials Science and Engineering B: Solid-State Materials for Advanced Technology*, 127(1), pp. 70–80. doi: 10.1016/j.mseb.2005.09.061.

Garofano, I. *et al.* (2011) 'Natural earth pigments from Roman and Arabic wall paintings revealed by spectroscopic techniques', *Spectroscopy Letters*, 44(7–8), pp. 560–565. doi: 10.1080/00387010.2011.610655.

Garofano, I., Robador, M. D. and Duran, A. (2014) 'Materials characteristics of Roman and Arabic mortars and stuccoes from the patio de banderas in the real alcazar of seville (Spain)', *Archaeometry*, 56(4), pp. 541–561. doi: 10.1111/arcm.12041.

Haschke, M. (2014) *Micro-X-Ray Fluorescence Spectroscopy - Instrumentation and*

Applications, *Springer-Verlag Berlin Heidelberg GmbH*. doi: 10.1007/978-3-319-04864-2.

Ippolito, A. (2017) 'Handbook of Research on Emerging Technologies for Digital Preservation and Information Modeling', i. doi: 10.4018/978-1-5225-0680-5.

Janssens, K. *et al.* (2013) 'The Use of Synchrotron Radiation for the Characterization of Artists' Pigments and Paintings', *Annual Review of Analytical Chemistry*, 6(1), pp. 399–425. doi: 10.1146/annurev-anchem-062012-092702.

Kanngießer, B. *et al.* (2012) 'A deep view in cultural heritage-confocal micro X-ray spectroscopy for depth resolved elemental analysis', *Applied Physics A: Materials Science and Processing*, 106(2), pp. 325–338. doi: 10.1007/s00339-011-6698-0.

Kanngießer, B., Malzer, W. and Reiche, I. (2003) 'A new 3D micro X-ray fluorescence analysis set-up - First archaeometric applications', *Nuclear Instruments and Methods in Physics Research, Section B: Beam Interactions with Materials and Atoms*, 211(2), pp. 259–264. doi: 10.1016/S0168-583X(03)01321-1.

Klockenkämper, R. and von Bohlen, A. (2015) *Total-Reflection X-Ray Fluorescence Analysis and Related Methods: Second Edition*, *Total-Reflection X-Ray Fluorescence Analysis and Related Methods: Second Edition*. doi: 10.1002/9781118985953.

Mahnke, H.-E. (2014) 'Nuclear Physics Methods in Cultural Heritage Research --- Accelerators for Art', *Acta Physica Polonica B*, 45(2), p. 571. doi: 10.5506/APhysPolB.45.571.

McGlinchey, C. (2012) 'Handheld XRF for the examination of paintings: Proper use and limitations', *Handheld XRF for Art and Archaeology*.

Musílek, L., Čechák, T. and Trojek, T. (2012) 'X-ray fluorescence in investigations of cultural relics and archaeological finds', *Applied Radiation and Isotopes*, 70(7), pp. 1193–1202. doi: 10.1016/j.apradiso.2011.10.014.

Nakano, K. and Tsuji, K. (2010) 'Development of laboratory confocal 3D-XRF spectrometer and nondestructive depth profiling', *Journal of Analytical Atomic Spectrometry*, 25(4), pp. 562–569. doi: 10.1039/b916974a.

Perez-Rodriguez, J. L. *et al.* (2015) 'Green pigments of Roman mural paintings from Seville Alcazar', *Applied Clay Science*. Elsevier B.V., 116–117, pp. 211–219. doi: 10.1016/j.clay.2015.03.016.

Siddall, R. (2006) 'Not a day without a line drawn: pigments and painting techniques of Roman Artists', *Focus Magazine: Proceedings of the Royal Microscopical Society*, 2, pp. 18–23. doi: 10.12659/AOT.893009.

Siddall, R. (2018) 'Mineral Pigments in Archaeology: Their Analysis and the Range of Available Materials', *Minerals*, 8(5), p. 201. doi: 10.3390/min8050201.

Wolff, T. *et al.* (2009) 'Performance of a polycapillary halflens as focussing and collecting optic - A comparison', *Journal of Analytical Atomic Spectrometry*, 24(5), pp. 669–675. doi: 10.1039/b817828c.

10 Table of tables

11 Table of figures